Seismo-hydro-mechanical modelling of the seismic cycle: Methodology and implications for subduction zone seismicity

Claudio Petrini[a,*], Taras Gerya[a], Viktoriya Yarushina[b], Ylona van Dinther[a,c], James Connolly[a], Claudio Madonna[a]

[a] *Department of Earth Sciences, ETH Zurich, Sonneggstrasse 5, 8092 Zurich, Switzerland*
[b] *Institute for Energy Technology, NO-2007 Kjeller, Norway*
[c] *Department of Earth Sciences, Utrecht University, 3584 CB Utrecht, Netherlands*

ABSTRACT

Slip accommodation in subduction zones ranges from aseismic slip phenomena to regular megathrust earthquakes, and strongly depends on pore fluid pressure. We develop a new fully coupled poro-visco-elasto-plastic seismo-hydro-mechanical numerical model, allowing for coupled modelling of tectonic and seismic processes in the presence of fluids. A combination of fully staggered finite differences and marker in cell techniques is used to solve mass and momentum conservation equations for solid matrix and fluid coupled to a poro-visco-elasto-plastic rheological constitutive relationship. Brittle/plastic deformation is resolved through global Picard-iterations and adaptive time stepping is introduced to resolve time scales from milliseconds to thousands of years involved in the hydro-mechanical seismic cycle.

We demonstrate how and why the presence of pervasive fluid flow in the deforming poro-visco-elasto-plastic subduction interface causes localisation of deformation and nucleation of seismic events with slip rate up to m/s. The nucleation of fault slip is controlled by rapid fluid pressure increase due to visco-plastic compaction of a spontaneously forming fault balanced by the simultaneous elastic decompaction of deforming pores inside the fault. Subsequent post- and inter-seismic slow fluid pressure release by elastic compaction of the stressed pores allows recovery of subduction interface strength. The events nucleate downdip in the brittle-ductile transition zone and propagate updip in form of highly localized, spontaneous ruptures. The model reproduces the broad spectrum of transient phenomena ranging from slow slip to seismic ruptures on a subduction interface with homogenous elastic and frictional properties that do not depend on slip rate. The degree of locking of the megathrust interface, the coseismic stress drop and the dominant slip regime during subduction are critically dependent on effective large-scale and long-term rock permeability. A decrease of permeability leads to a decrease of degree of locking, leading to smaller stress drop and enhancing the occurrence of stable aseismic slip.

1. Introduction

Subduction zones show a high degree of seismicity and account for more than 90% of the global seismic moment release [Pacheco and Sykes, 1992]. Many regions along subduction zones are densely populated and a better understanding of why and how subduction-induced earthquakes happen and which mechanisms trigger and control seismicity may improve seismic hazard assessment in those regions. Subduction zone seismicity is broadly variable in origin and is represented by both regular earthquakes and slow slip phenomena of variable magnitude [e.g., Ide et al., 2007; Peng and Gomberg, 2010]. The exact physical mechanisms responsible for this broad variability are under

debate [e.g., Poulet et al., 2014 and references therein] as are also the roles of pressured fluids derived from subducting slabs in earthquake generation [Beroza and Ide, 2009; Obara, 2002; Poulet et al., 2014; Saffer and Wallace, 2015]. It has been hypothesized that both regular earthquakes and slow slip phenomena in subduction zones are intrinsically related to fluid transport processes [e.g., Audet and Schwartz, 2013; Brown et al., 2005; Moreno et al., 2014 and references therein; Poulet et al., 2014; Saffer and Tobin, 2011; van Dinther et al., 2013b; Yamashita and Suzuki, 2011]. Fluid pressure, in particular, imposes critical controls on the degree of interseismic locking and hydro-mechanical heterogeneity of the subduction interface [Moreno et al., 2014; Moreno et al., 2018] thereby affecting seismic cycle

---

behaviour [e.g., Gao and Wang, 2017; van Dinther et al., 2013b]. Fluid flow and pressure are also responsible for different types of seismicity in other tectonic and environmental settings. In particular, seismic activity in active volcanic system and induced seismicity triggered by fluid injections are directly controlled by fluid-rock interactions [Koulakov et al., 2013; Shapiro, 2015; Shapiro and Dinske, 2009; Shapiro et al., 2003; Yarushin et al., 2017], highlighting the importance of understanding the physics of fluid-rock interaction processes for understanding seismicity.

Due to limited direct observations in time and space, understanding of broadly variable subduction zone seismicity also requires knowledge transfer from other disciplines, such as reservoir sciences and geomechanics, and significant numerical modelling effort [e.g., Duan and Oglesby, 2005; Herrendörfer et al., 2015 and references therein; Kaneko et al., 2010; Lapusta et al., 2000; Liu and Rice, 2009; Mitsui et al., 2012; Noda and Lapusta, 2010; Poulet et al., 2014; Rutqvist et al., 2018; van Dinther et al., 2013a; van Dinther et al., 2013b; van Dinther et al., 2014; KWang et al., 2012]. Numerical approaches provide additional quantitative constraints and offer a robust way of testing different physical hypotheses for seismicity dynamics, controls and triggering [e.g., Dal Zilio et al., 2018; Herrendörfer et al., 2015 and references therein]. Wang [2007] identified three key features that should be combined for a complete numerical model of subduction seismicity: (1) a rate-dependent friction, (2) slow tectonic loading and (3) visco-elastic stress relaxation. Taking into account the critical significance of fluids for seismicity, an additional key numerical modelling requirement for this is (4) self-consistent seismo-hydro-thermo-mechanical coupling of rock deformation and fluid transport processes [e.g., Dymkova and Gerya, 2013; Gao and Wang, 2017; Poulet et al., 2014; van Dinther et al., 2013b].

Several numerical methods were developed and applied to understand seismicity along subduction zones [e.g., Duan and Oglesby, 2005; Gao and Wang, 2017; Herrendörfer et al., 2015 and references therein; Kaneko et al., 2010; Lapusta and Liu, 2009; Liu and Rice, 2007; van Dinther et al., 2013a; van Dinther et al., 2013b; van Dinther et al., 2014; KWang et al., 2012]. Beside geodetic measurements and field observations, which have limitations in completeness and quantity, numerical models can improve significantly the understanding of the driving physics of seismic cycles and increase accuracy in seismic hazard assessment and tsunamigenesis. Recently, many improvements were made in modelling subduction zone seismicity [e.g., Duan and Oglesby, 2005; Gao and Wang, 2017; Herrendörfer et al., 2015; Lapusta and Liu, 2009; van Dinther et al., 2013a; van Dinther et al., 2013b; van Dinther et al., 2014; KWang et al., 2012 and references therein] and in particular new continuum-based approaches have been proposed and validated [Herrendörfer et al., 2018; Sobolev and Muldashev, 2017; van Dinther et al., 2013a; van Dinther et al., 2013b]. These new approaches are able to model various seismic cycles on large-scale subduction and collision zone setups [Dal Zilio et al., 2019; Dal Zilio et al., 2018; Herrendörfer et al., 2015; van Dinther et al., 2013a; van Dinther et al., 2013b; van Dinther et al., 2014]. Furthermore, they were able to model complex spatial and temporal distribution of earthquakes in convergent systems [van Dinther et al., 2014] and to produce realistic Gutenberg-Richter relationship in collisional regions [Dal Zilio et al., 2018]. Recently this numerical approach was further improved by implementing rate and state friction (RSF) and an adaptive time stepping algorithm to enable an accurate transition from geological time scales (kyr to Myr) to seismic time scales (milliseconds to hours) and increasing the spectrum of modelled seismic events from aseismic slip, to slow-slip phenomena and to regular seismic events [Gerya, 2019; Herrendörfer et al., 2018].

It has been suggested that the presence of fluids in the subduction plate play a crucial role both on long-term as well as on seismic time scales [e.g., Gao and Wang, 2017; Saffer and Tobin, 2011; van Dinther et al., 2013b]. Many studies were carried out to understand fluid processes in subduction zones [e.g., Cagnioncle et al., 2007; Dymkova and Gerya, 2013; Iwamori, 1998, 2000, 2007; Wilson et al., 2014] and a

wealth of theoretical work is available to better understand the physics of rock-fluid interactions and processes in porous media with different rheologies [e.g., Connolly and Podladchikov, 1998; Keller et al., 2013; McKenzie, 1984; Spiegelman, 1993; Stevenson and Scott, 1991; Yarushina and Minakov, 2018; Yarushina and Podladchikov, 2015]. In particular, several studies addressed porosity evolution and (de)compaction of reologically complex visco-(elasto)-plastic porous media, particularly focusing on fluid transport throughout the asthenosphere and lithosphere through propagation of porosity waves, emphasising the importance of fluid transport in porous media in geodynamics [e.g., Connolly and Podladchikov, 2000; Connolly and Podladchikov, 2007, 2015; Dymkova and Gerya, 2013; Keller et al., 2013; Yarushina and Podladchikov, 2015; Yarushina et al., 2015]. Fluid influence on short-term seismic processes has also been actively explored [e.g., Audet and Schwartz, 2013; Husen and Kissling, 2001; Moreno et al., 2014 and references therein; Shapiro, 2015; Shapiro and Dinske, 2009; Shapiro et al., 2003; Tassara et al., 2016] and several studies were carried out on coupled hydro-mechanical (HM) modelling to investigate seismic activity, rupture dynamics and fault mechanics [Garagash, 2012; Mitsui et al., 2012; Noda and Lapusta, 2010; Poulet et al., 2017; Viesca et al., 2008]. Rice [1992] addressed the role of fluid pressure as a weakening factor for the San Andreas Fault and described fluid flow in porous media as a possible source for fluid in a fault system. Recent studies focused on fluid influence on slow slip phenomena [e.g., Gao and Wang, 2017; Nakajima and Uchida, 2018; Poulet et al., 2014 and references therein; Yamashita and Suzuki, 2011]. Furthermore, Skarbek and Rempel [2016] investigated with numerical models how porosity waves induced by dehydration reactions can be related to episodic tremor and slip (ETS).

Despite the steady progress in understanding of fluid pressure influences on seismicity, to our knowledge, no continuum-based fully coupled seismo-hydro-mechanical (SHM) subduction seismicity model has been developed yet that considers both realistic poro-visco-elasto-plastic rock rheology and influences of local fluid pressure variations on the rock strength. In this paper, we develop such new fully coupled 2D SHM approach based on staggered finite differences and marker-in-cell techniques (SFD + MIC, [Gerya, 2019]). This SHM approach is able to reproduce seismic cycles in a poro-visco-elasto-plastic medium, by coupling inertia, rock strength and deformation with fluid flow. This numerical approach treats accurately poro-visco-elasto-plastic deformation by applying global iterative procedure and resolving fluid pressure-dependent yield strength with high numerical accuracy. We use an adaptive time stepping procedure to model both long-term deformation and seismic events with a time resolution up to milliseconds.

We use this new numerical SHM tool to demonstrate that seismic cycles in subduction zones could also be potentially induced by fluid pressure variations alone without incorporation of rate- (and state-) dependent friction. We furthermore investigate the role of poro-elasticity on the accumulation and release of elastic stress, as similarly done in a number of previous studies [eg., Ge and Screaton, 2005; Hughes et al., 2010; LaBonte et al., 2009], thereby defining the physical mechanism of the hydro-mechanical seismic cycle. The method section presents the numerical approach, describing the hydro-mechanical conservation equations and the poro-visco-elasto-plastic rheological constitutive relationship. The results section describes the numerical model of subduction and results of several reference simulations with the focus on understanding the physics of the hydro-mechanical coupling that generates seismicity. The discussion section examines then main implications of this study and outlines directions for further methodological improvements.

2. Methods

This section describes the governing equations and the fully coupled seismo-hydro-mechanical poro-visco-elasto-plastic numerical modelling approach based on staggered finite differences with marker-in-cell

techniques, global Picard iterations and adaptive time stepping [Gerya, 2019; Gerya and Yuen, 2007]. We implement self-consistent fluid-solid coupling in a fully inertial poro-visco-elasto-plastic (de)compacting medium based on the poroelastic theory developed by Biot [1941, 1956a, 1956b] and on the visco-plastic model described by Dymkova and Gerya [2013], while using the mathematical model formulation presented by Yarushina and Podladchikov [2015]. Thermal component is neglected at this stage, but could be added relatively easily [e.g., Gerya, 2019; McKenzie, 1984].

2.1. Conservation equations

Total momentum (i.e., for the bulk material consisting of solid matrix and fluid) (Eq. (1)), solid mass (Eq. (2)), fluid momentum (Eq. (3)) and fluid mass (Eq. (4)) conservation equations are formulated in a thermodynamically consistent manner as [Gerya, 2019; Yarushina and Podladchikov, 2015]

$$\frac{\partial \sigma'_{ij}}{\partial x_j} - \frac{\partial p^t}{\partial x_i} + \rho^t g_i = (1 - \varphi)\rho^s \frac{D^s v_i^s}{Dt} + \varphi \rho^s \frac{D^f v_i^f}{Dt} \tag{1}$$

$$\nabla \cdot v^s = -\frac{1}{K^d}\left(\frac{D^s p^t}{Dt} - \alpha \frac{D^f p^f}{Dt}\right) - \frac{p^t - p^f}{\eta^\varphi(1 - \varphi)} \tag{2}$$

$$v_i^D = -\frac{k}{\eta^f}\left(\nabla p^f - \rho^f g_i + \rho^f \frac{D^f v_i^f}{Dt}\right) \tag{3}$$

$$\nabla \cdot v^D = \frac{\alpha}{K^d}\left(\frac{D^s p^t}{Dt} - \frac{1}{\beta}\frac{D^f p^f}{Dt}\right) + \frac{p^t - p^f}{\eta^\varphi(1 - \varphi)} \tag{4}$$

By neglecting differences (that occurred to be very small in our numerical experiments) in acceleration of solid and fluid (i.e. by assuming $\frac{D^f v_i^f}{Dt} \approx \frac{D^s v_i^s}{Dt}$) the following simplified inertia terms are used in Eqs. (1) and (3):

$$\varphi \rho^f \frac{D^f v_i^f}{Dt} + (1 - \varphi)\rho^s \frac{D^s v_i^s}{Dt} \approx \rho^t \frac{D^s v_i^s}{Dt} \tag{5}$$

$$\rho^f \frac{D^f v_i^f}{Dt} \approx \rho^f \frac{D^s v_i^s}{Dt} \tag{6}$$

where superscripts *f*, *s* and *t* respectively stand for fluid, solid matrix and total properties. φ is the connected porosity (rocks can also contain isolated pores, which do not affect fluid flow and are therefore treated as part of the solid matrix in our formulation), $p^t = p^f \varphi + p^s(1 - \varphi)$ and $\rho^t = \rho^f \varphi + \rho^s(1 - \varphi)$ are respectively the total pressure and density computed from respective fluid and solid matrix quantities, σ_{ij}' is the deviatoric stress for the bulk material, v_i^s and v_i^f are the *i*-th component of the solid and fluid velocities, v_i^D is the *i*-th component of Darcy's velocity, which is defined as $\varphi(v_i^f - v_i^s)$, *k* is the permeability, η^f is the fluid viscosity, g_i is the *i*-th gravity component, $\frac{D^s}{Dt}$ and $\frac{D^f}{Dt}$ represent the Lagrangian time derivative in the solid and fluid reference frame, respectively. η^φ is the effective compaction viscosity, which can be expressed as [Yarushina and Podladchikov, 2015]:

$$\eta^\varphi = \frac{2m}{(m+1)}\frac{\eta^s}{\varphi} \tag{7}$$

where *m* is a geometrical factor, being 1 for cylindrical pores and 2 for spherical pores [Yarushina and Podladchikov, 2015], η^s is the shear viscosity of the solid matrix. The parameter α is the Biot-Willis coefficient [Yarushina and Podladchikov, 2015]:

$$\alpha = 1 - \frac{K^d}{K^s} \tag{8}$$

with K^s being the solid bulk modulus and K^d the drained bulk modulus [Yarushina and Podladchikov, 2015]:

$$K^d = (1 - \varphi)\left(\frac{1}{K^\varphi} + \frac{1}{K^s}\right)^{-1} \tag{9}$$

with K^φ the effective bulk modulus of pores [Yarushina and Podladchikov, 2015]:

$$K^\varphi = \frac{2m}{(m+1)}\frac{G}{\varphi} \tag{10}$$

where *G* is the shear modulus. The Skempton's coefficient β is given by [Yarushina and Podladchikov, 2015]:

$$\beta = \frac{\frac{1}{K^d} - \frac{1}{K^s}}{\frac{1}{K^d} - \frac{1}{K^s} + \varphi\left(\frac{1}{K^f} - \frac{1}{K^s}\right)} \tag{11}$$

where K^f is the fluid bulk modulus.

In majority of our numerical calculations, fluid inertial term $\rho^f \frac{D^f v_i^f}{Dt}$ in Eq. (3) is neglected, assuming that inertial forces do not significantly affect fluid percolation and Eq. (3) can be simplified to:

$$v_i^D = -\frac{k}{\eta^f}(\nabla p^f - \rho^f g_i) \tag{12}$$

In the solid momentum equation, the inertia term is always present and allows for the ruptures to reach seismic velocities.

The two continuity equations contain poroelasticity terms [Yarushina and Podladchikov, 2015] which allows for compressibility of the solid and fluid, as well as viscous and elastic compaction of the interconnected porous space. To simplify the solving of equations and to explore the fluid pressure related feedback between the elastic and visco-plastic (de)compaction of pores in a simplified manner, the solid and fluid are assumed to be incompressible ($\frac{1}{K^s} = \frac{1}{K^f} = 0$ and consequently $\alpha = \beta = 1$), whereas elastic compressibility of pores related to $\frac{1}{K^\varphi}$ remains non-zero. This leads to some simplifications in the solid and fluid mass conservation Eqs. (2) and (4), resulting respectively in:

$$\nabla \cdot v^s = -\frac{1}{K^\varphi(1 - \varphi)}\left(\frac{D^s p^t}{Dt} - \frac{D^f p^f}{Dt}\right) - \frac{p^t - p^f}{\eta^\varphi(1 - \varphi)} \tag{13}$$

$$\nabla \cdot v^D = \frac{1}{K^\varphi(1 - \varphi)}\left(\frac{D^s p^t}{Dt} - \frac{D^f p^f}{Dt}\right) + \frac{p^t - p^f}{\eta^\varphi(1 - \varphi)} \tag{14}$$

Eqs. (13) and (14) couple together the solid and fluid phase reflecting convergence/divergence of the solid matrix, respectively the fluid, in response to local compaction/decompaction processes, forming a fully coupled hydro-mechanical system. Eqs. (13) and (14) will interact in the described manner irrespective of whether fluid/solid incompressibility assumption is applied or not and describe classical behaviour of a (de)compacting coupled incompressible fluid-solid system that is described in many previous works [Gerya, 2019 and references therein; McKenzie, 1984; Spiegelman, 1993; Yarushina and Podladchikov, 2015]. Our preliminary tests have shown that taking into account fluid and solid compressibility does not change the pores pressurization mechanism and seismic behaviour of the models but increases drastically the number of time steps needed to resolve the coseismic phase (due to appearance of pressure waves).

2.2. Solid matrix rheology

The strain rate tensor is defined as follows:

$$\dot{\varepsilon}_{ij} = \frac{1}{2}\left(\frac{\partial v_i^s}{\partial x_j} + \frac{\partial v_j^s}{\partial x_i}\right) \tag{15}$$

and by subtracting its isotropic part $\dot{\varepsilon}_{kk} = div(\overrightarrow{v}^s)$ the deviatoric strain rate tensor is found:

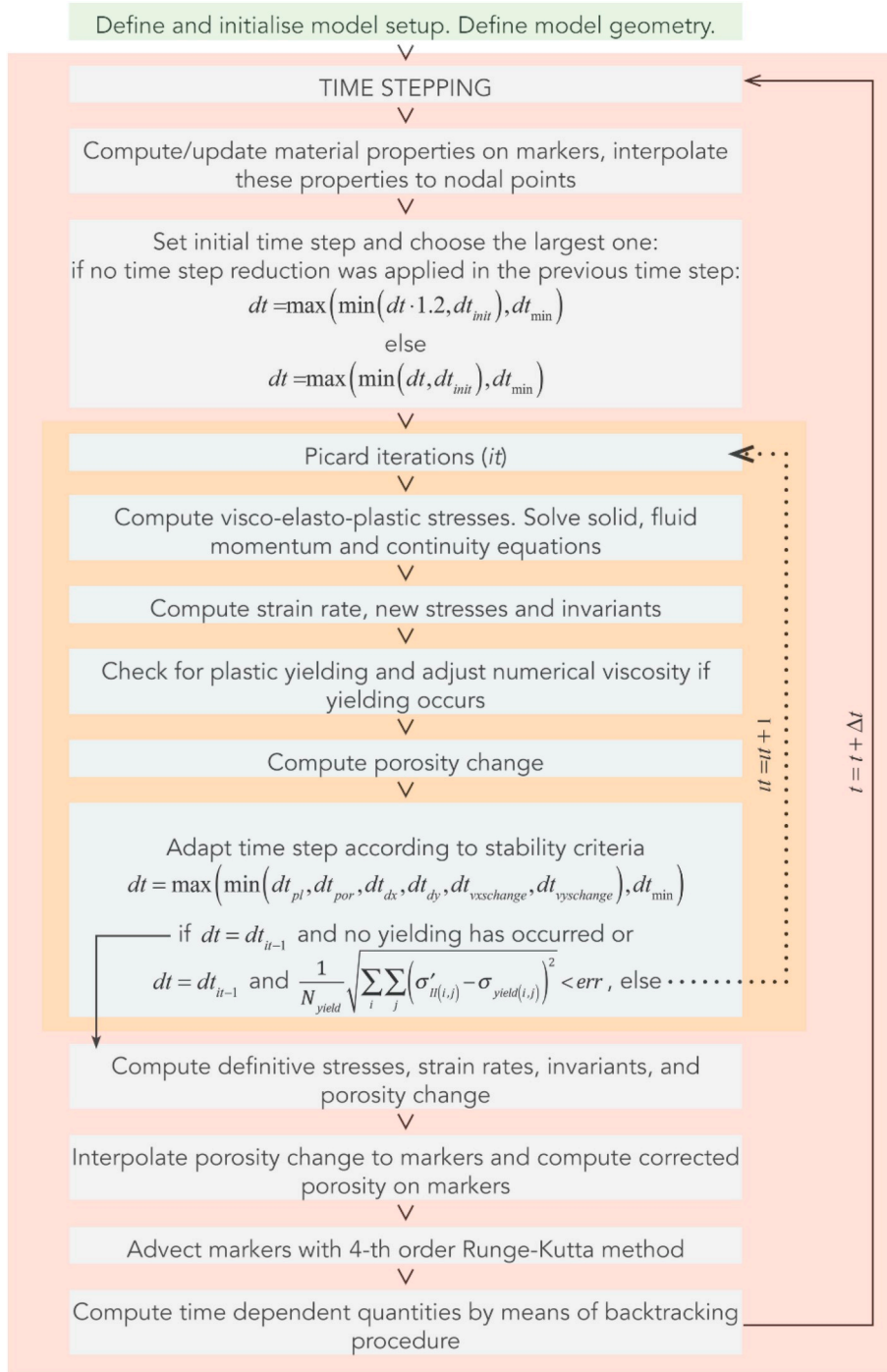$$\dot{\varepsilon}_{ij}' = \dot{\varepsilon}_{ij} - \frac{1}{3}\dot{\varepsilon}_{kk}\delta_{ij} \tag{16}$$

Define and initialise model setup. Define model geometry.

∨

TIME STEPPING

∨

Compute/update material properties on markers, interpolate these properties to nodal points

∨

Set initial time step and choose the largest one:
if no time step reduction was applied in the previous time step:

$$dt = \max\left(\min\left(dt \cdot 1.2, dt_{init}\right), dt_{min}\right)$$

else

$$dt = \max\left(\min\left(dt, dt_{init}\right), dt_{min}\right)$$

∨

Picard iterations (it)

∨

Compute visco-elasto-plastic stresses. Solve solid, fluid momentum and continuity equations

∨

Compute strain rate, new stresses and invariants

∨

Check for plastic yielding and adjust numerical viscosity if yielding occurs

∨

Compute porosity change

∨

Adapt time step according to stability criteria

$$dt = \max\left(\min\left(dt_{pl}, dt_{por}, dt_{dx}, dt_{dy}, dt_{vxschange}, dt_{vyschange}\right), dt_{min}\right)$$

if $dt = dt_{it-1}$ and no yielding has occurred or

$$dt = dt_{it-1} \text{ and } \frac{1}{N_{yield}}\sqrt{\sum_i \sum_j \left(\sigma'_{II(i,j)} - \sigma_{yield(i,j)}\right)^2} < err \text{, else}$$

∨

Compute definitive stresses, strain rates, invariants, and porosity change

∨

Interpolate porosity change to markers and compute corrected porosity on markers

∨

Advect markers with 4-th order Runge-Kutta method

∨

Compute time dependent quantities by means of backtracking procedure

$it = it + 1$

$t = t + \Delta t$

Fig. 1. Structure describing the code algorithm. The red box shows the sequence of steps during each timestep. The yellow box represents the cycle of the *Picard iterations* inside each time step, needed to adjust stresses and strain rates and adapt the time step (dt) to the suitable time interval. dt_{init} is the time step defined initially, dt_{min} is the minimal allowed time step, whereas dt_{pl}, dt_{por}, dt_{dx}, dt_{dy}, $dt_{vxschange}$ and $dt_{vyschange}$ are the timesteps that satisfy plastic yielding convergence, maximal porosity change, maximal x and y displacements and maximal x and y velocity changes per time step, respectively. (For interpretation of the references to colour in this figure legend, the reader is referred to the web version of this article.)

We used a standard visco-elasto-plastic Maxwell rheology model with Drucker-Prager yielding criterion affected by the difference between the total and fluid pressure [e.g., Gerya, 2019; Ranalli, 1995] for the bulk material considered in the solid strain rate reference frame:

$$\dot{\varepsilon}'_{ij} = \frac{1}{2}\left(\frac{\partial v_i^s}{\partial x_j} + \frac{\partial v_j^s}{\partial x_i}\right) - \delta_{ij}\frac{1}{3}div\left(\vec{v}^s\right) = \dot{\varepsilon}'_{ij(viscous)} + \dot{\varepsilon}'_{ij(elastic)} + \dot{\varepsilon}'_{ij(plastic)}$$

(17)

with

$$\dot{\varepsilon}'_{ij(viscous)} = \frac{1}{2\eta}\sigma'_{ij}$$

(18)

$$\dot{\varepsilon}'_{ij(elastic)} = \frac{1}{2G}\frac{D^s\sigma'_{ij}}{Dt}$$

(19)

$$\dot{\varepsilon}'_{ij(plastic)} = \begin{cases} 0 & \text{for } \sigma'_{II} < \sigma_{yield} \\ \chi\frac{\partial Q}{\partial \sigma'_{ij}} = \chi\frac{\sigma'_{ij}}{2\sigma'_{II}} & \text{for } \sigma'_{II} = \sigma_{yield} \end{cases}$$

(20)

where v_{ij}^s is the velocity of the solid, η and G are the effective shear viscosity and shear modulus of the bulk material, $\frac{D^s\sigma'_{ij}}{Dt}$ the co-rotational derivative of the deviatoric stress tensor, χ is a plastic multiplier, which has to fulfil the Drucker-Prager yielding criterion $\sigma_{II}' = \sigma_{yield}$ [Drucker and Prager, 1952; Gerya, 2019], σ_{II}' the square root of the second

invariant of the deviatoric stress tensor, $Q = \sigma_{II}'$ is the plastic potential, whereas σ_{yield} is the yield stress, i.e. the maximal deviatoric stress rock can sustain (see Eq. (22)). The plastic multiplier χ, obtained algebraically from Eq. (20), is equal to the double of the square root of the second invariant of the deviatoric plastic strain rate (see appendix for full derivation):

$$\chi = 2\dot{\varepsilon}_{II\,(plastic)} \qquad (21)$$

To simplify the implementation of the visco-elasto-plastic rheology in a straight-forward manner, a viscosity-like reformulation of the rheology is applied following Gerya [2019] (see appendix for full derivation).

We also assumed that the Drucker-Prager yielding condition depends on total and fluid pressure as [Gerya, 2019]:

$$\sigma_{yield} = \min[\sigma_c + \mu(p^t - p^f), \sigma_t + (p^t - p^f)] = \sigma_{II}' \qquad (22)$$

where σ_c and σ_t are respectively the compressive and tensile strength of the bulk material (we used $\sigma_c = \sigma_t$ condition in our experiments), μ is the internal friction coefficient. It should be stressed that pore pressure evolution imposes a major control on the rock yield strength evolution, since the latter is assumed to be dependent on effective pressure $p_e = (p^t - p^f)$. Change in fluid pressure acts as strengthening or weakening factor controlling the strength [e.g., Jaeger et al., 2007; Rice, 1992; Sibson, 1990; Sleep and Blanpied, 1994] and the brittle/plastic behaviour of the material in both compressive and tensile mode of the deformation.

A visco-plastic viscosity-like parameter η^{vp}, which includes both plastic and viscous deformation, can be defined [Gerya, 2019] (see appendix for full derivation):

$$\eta^{vp} = \eta \ \textbf{\textit{for}} \ \sigma_{II}' < \sigma_{yield}$$

$$\eta^{vp} = \eta \frac{\sigma_{II}'}{\sigma_{II}' + \chi\eta} = \eta \frac{\sigma_{II}'}{\sigma_{II}' + 2\dot{\varepsilon}_{II\,(plastic)}\eta} \ \textbf{\textit{for}} \ \sigma_{II}' = \sigma_{yield} \qquad (23)$$

Leading to a viscosity-like reformulation for the sum of plastic and viscous deviatoric strain rate in Eq. (17):

$$\dot{\varepsilon}_{ij\,(viscoplastic)}' = \dot{\varepsilon}_{ij\,(viscous)}' + \dot{\varepsilon}_{ij\,(plastic)}' = \frac{1}{2\eta^{vp}}\sigma_{ij}' \qquad (24)$$

The introduction of a viscous approximation of plasticity is robust both mathematically and numerically [e.g., Gerya, 2019; Herrendörfer et al., 2018] and does not introduce additional time scales as long as an adaptive time stepping is applied (Section 2.3 and Fig. 1) and no minimum cut-off viscosity limit is imposed [Herrendörfer et al., 2018]. A good correspondence between the continuum-based approach and dynamic rupture simulations has been recently demonstrated [Herrendörfer et al., 2018].

Finally, using Eqs. (17) and (24) the visco-elasto-plastic stress relation can be obtained in a time-discretized form [Gerya, 2019] (see appendix for full derivation):

$$\sigma_{ij}' = 2\eta^{vp}\dot{\varepsilon}_{ij}'Z + \sigma_{ij}'^0(1 - Z) \qquad (25)$$

$$Z = \frac{G\Delta t}{G\Delta t + \eta^{vp}} \qquad (26)$$

where $\sigma_{ij}'^0$ is the deviatoric stress of the previous time step, Z is visco-elasticity factor, Δt is the computational time step.

2.2.1. Porosity evolution and porosity dependent material properties

To account for pore space volume change, an interconnected porosity evolves (in the Lagrangian solid matrix velocity frame) accordingly to changes in total and fluid pressure as well as compression of the fluid and solid matrix [Gerya, 2019; Yarushina and Podladchikov, 2015].

$$\frac{D^s \ln(1 - \varphi)}{Dt} = \frac{1}{K^\varphi(1 - \varphi)}\left(\frac{D^s p^t}{Dt} - \frac{D^f p^f}{Dt}\right) + \frac{p^t - p^f}{\eta^\varphi(1 - \varphi)} \qquad (27)$$

A porosity dependent permeability is implemented as:

$$k = k^0\left(\frac{\varphi}{\varphi^0}\right)^n \qquad (28)$$

where n is an exponent that can vary significantly (from 1 up to 50) depending on the porosity dependence of permeability [Yarushina et al., 2013]. Geometrically defined values are between 2 and 3, where for a natural pore distribution this exponent is taken to be 3 [Connolly and Podladchikov, 2000; Dymkova and Gerya, 2013; Morency et al., 2007; Rice, 1992], changing the permeability as a cube of increasing porosity. k^0 is the reference permeability and φ^0 the reference porosity, which is set to be 0.01 (i.e. 1%).

A porosity dependent shear modulus of the bulk material is used [Mavko et al., 2009; Wang, 1984]:

$$G = G^0\left(1 - \frac{\varphi}{\varphi_{crit}}\right) \qquad (29)$$

with G^0 the shear modulus of solid rock grains and φ_{crit} a rock specific critical porosity (or disaggregation porosity, which is not reached in our numerical experiments), at which the rock start to disaggregate and become a suspension [Connolly and Podladchikov, 2015; Mavko et al., 2009]. The same rule applies for compressive and tensile strength of the bulk material [Wong and Baud, 2012; Yarushina and Podladchikov, 2015]:

$$\sigma_c = \sigma_{c0}\left(1 - \frac{\varphi}{\varphi_{crit}}\right) \qquad (30)$$

$$\sigma_t = \sigma_{t0}\left(1 - \frac{\varphi}{\varphi_{crit}}\right) \qquad (31)$$

where σ_{c0} and σ_{t0} are respectively the compressive and tensile strength of the pure solid.

For shear viscosity of the bulk material we chose to use an exponential porosity dependent formulation presented in Schmeling et al. [2012] and Keller et al. [2013], which is a simplification of a more complex law suggested by Katz et al. [2006]:

$$\eta = \eta^s e^{\alpha_\nu \varphi} \qquad (32)$$

where η^s is the solid grain shear viscosity, $\alpha_\nu = -28 \pm 3$ is an experimentally derived porosity-weakening factor. Eq. (32) is valid for relatively low fluid fractions used in our numerical experiments i.e., $\varphi < \varphi_{crit}$.

2.3. Adaptive time stepping and global Picard iterations

It is known that numerical implementation of nonlinear equations is challenging. To be able to accurately solve the equations and resolve each individual seismic event with many time steps, an adaptive time stepping is formulated. Global *Picard iterations* are performed to reach convergence of the numerical solution within an a-priori defined high-accuracy level. Furthermore, the adaptive time stepping helps the convergence of the *Picard iterations* [e.g., Gerya, 2019].

After solving the governing equations on the Eulerian grid and checking for the yielding conditions, the time step is computed in such a way that porosity changes, displacement and velocity changes are
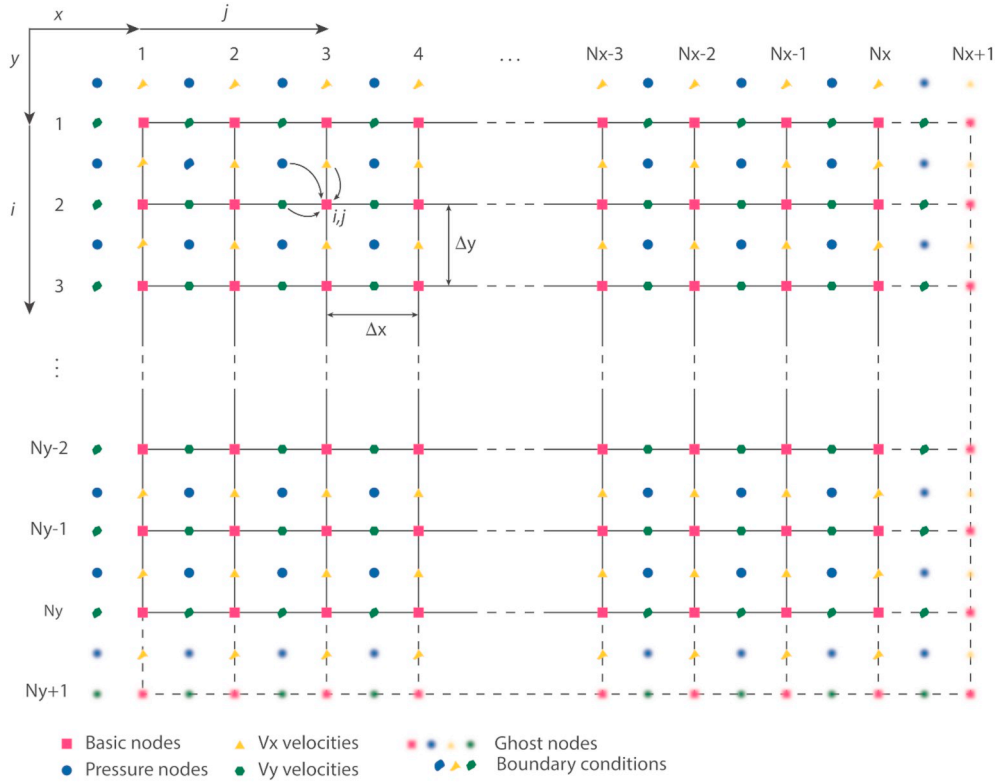
Fig. 2. Fully staggered grid with representation of the different nodes, boundary conditions and ghost nodes. The ghost nodes are not used in conservation and boundary condition equations, but add uniformity of indexing of unknowns within the grid to the numerical implementation [Gerya, 2019].

below predefined limiting values (Fig. 1, yellow box), which ensure stability and convergence of the numerical solution. Furthermore, time stepping is also adjusted for satisfying accurately the plastic yielding condition (Eq. (22)). To satisfy this condition within a pre-defined accuracy level we implemented global visco-elasto-plastic *Picard iterations* on Eulerian nodes [Gerya, 2019; Herrendörfer et al., 2018]. If plastic yielding occurs and the yielding stress condition is not resolved within a pre-defined given number of iterations, the time step is decreased, viscoplastic viscosity is corrected and *Picard iterations* are carried out from the beginning of the time step by solving again the governing equations on Eulerian nodes with a smaller time step size and the corrected visco-elasto-plastic stresses (Fig. 1, yellow box). Once the yielding condition accuracy criterion is met as well as all the stability criteria, *Picard iterations* are stopped, and the computation is carried on, continuing to the next time step. Performing *Picard iterations* and adapting the time step allow resolving accurately, both in space and time, brittle/plastic deformation and stress state under conditions of evolving effective pressure. This allows the shear zone nucleation, lateral propagation, arrest and strength evolution to be well resolved. This approach also guarantees through following of changes in the brittle/plastic rock strength before, during and after the seismic events (i.e. at all stages of the seismic cycle).

2.4. Discretization of the basic equations

The equations are solved on a 2D fully staggered Eulerian grid (Fig. 2) with *Nx* and *Ny* number of nodes in the *x*- and *y*-direction respectively.

The different variables are fully staggered on the grid as shown in Fig. 3 to ensure optimal discretization of the 2D momentum and mass conservation equations [Gerya, 2019].
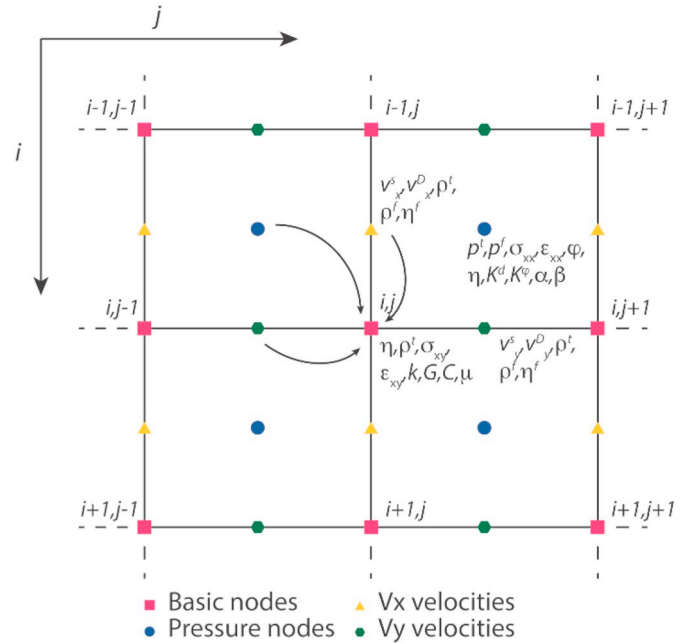

Fig. 3. Distribution of variables on the different nodes. Black arrows indicate indexing of staggered nodes.

Fig. 4a and b represent the stencils used to discretise the momentum conservation equation (Eq. (1)) formulated for respectively *x* and *y* solid matrix velocity components by including Eqs. (15) and (25) in Eq. (1)
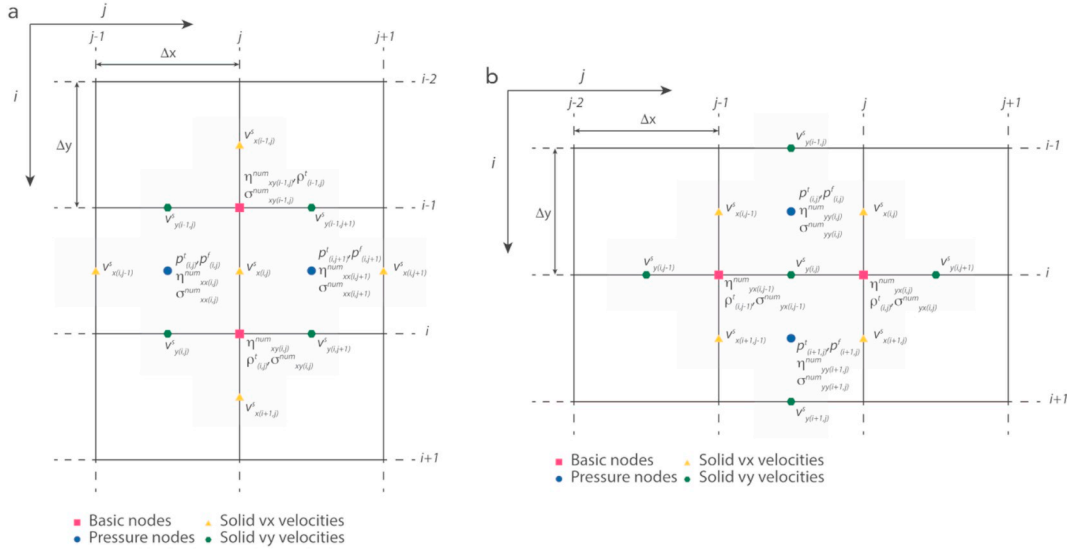
Fig. 4. Stencils for discretising the momentum equation for the bulk material. a) *x*-momentum equation (Eq. (1)) and b) *y*- momentum equation (Eq. (1)).

$$\left(\frac{\eta^{num}_{xx(i,j+1)}(v^s_{x(i,j+1)} - v^s_{x(i,j)})}{dx^2} - \frac{\eta^{num}_{xx(i,j)}(v^s_{x(i,j)} - v^s_{x(i,j-1)})}{dx^2}\right) - \Big($$

$$\frac{\eta^{num}_{xx(i,j+1)}(v^s_{y(i,j+1)} - v^s_{y(i-1,j+1)})}{dxdy} - \frac{\eta^{num}_{xx(i,j)}(v^s_{y(i,j)} - v^s_{y(i-1,j)})}{dxdy}\Big)$$

$$+\left(\frac{\eta^{num}_{xy(i,j)}(v^s_{x(i+1,j)} - v^s_{x(i,j)})}{dy^2} - \frac{\eta^{num}_{xy(i-1,j)}(v^s_{x(i,j)} - v^s_{x(i-1,j)})}{dy^2}\right) + \Big($$

$$\frac{\eta^{num}_{xy(i,j)}(v^s_{y(i,j+1)} - v^s_{y(i,j)})}{dydx} - \frac{\eta^{num}_{xy(i-1,j)}(v^s_{y(i-1,j+1)} - v^s_{y(i-1,j)})}{dydx}\Big)$$

$$-\frac{(p^t_{(i,j+1)} - p^t_{(i,j)})}{dx} + \rho^t g_x$$

$$= \rho^t \frac{(v^s_{x(i,j)} - v^{s0}_{x(i,j)})}{dt} - \left(\frac{\sigma^{num}_{xx(i,j+1)} - \sigma^{num}_{xx(i,j)}}{dx}\right) - \left(\frac{\sigma^{num}_{xy(i,j)} - \sigma^{num}_{xy(i-1,j)}}{dy}\right)$$

(33)

$$\left(\frac{\eta^{num}_{yy(i+1,j)}(v^s_{y(i+1,j)} - v^s_{y(i,j)})}{dy^2} - \frac{\eta^{num}_{yy(i,j)}(v^s_{y(i,j)} - v^s_{y(i-1,j)})}{dy^2}\right) - \Big($$

$$\frac{\eta^{num}_{yy(i+1,j)}(v^s_{x(i+1,j)} - v^s_{x(i+1,j-1)})}{dydx} - \frac{\eta^{num}_{yy(i,j)}(v^s_{x(i,j)} - v^s_{x(i,j-1)})}{dydx}\Big)$$

$$+\left(\frac{\eta^{num}_{yx(i,j)}(v^s_{x(i+1,j)} - v^s_{x(i,j)})}{dxdy} - \frac{\eta^{num}_{yx(i,j-1)}(v^s_{x(i+1,j-1)} - v^s_{x(i,j-1)})}{dxdy}\right) + \Big($$

$$\frac{\eta^{num}_{yx(i,j)}(v^s_{y(i,j+1)} - v^s_{y(i,j)})}{dx^2} - \frac{\eta^{num}_{yx(i,j-1)}(v^s_{y(i,j)} - v^s_{y(i,j-1)})}{dx^2}\Big)$$

$$-\frac{(p^t_{(i+1,j)} - p^t_{(i,j)})}{dy} + \rho^t g_y$$

$$= \rho^t \frac{(v^s_{y(i,j)} - v^{s0}_{y(i,j)})}{dt} - \left(\frac{\sigma^{num}_{yy(i+1,j)} - \sigma^{num}_{yy(i,j)}}{dy}\right) - \left(\frac{\sigma^{num}_{yx(i,j)} - \sigma^{num}_{yx(i,j-1)}}{dx}\right)$$

(34)

where $\eta^{num} = \eta^{vp}Z$, $\sigma_{xx}{}^{num} = \sigma'_{xx}{}^0(1 - Z)$, $\sigma_{yy}{}^{num} = \sigma'_{yy}{}^0(1 - Z)$ and $\sigma_{xy}{}^{num} = \sigma_{yx}{}^{num} = \sigma'_{xy}{}^0(1 - Z)$.

Fig. 5a and b represent the stencils used to discretize the mass conservation Eqs. (13 and 14), solved for respectively solid matrix and fluid:

$$\frac{(v^s_{x(i,j)} - v^s_{x(i,j-1)})}{dx} + \frac{(v^s_{y(i,j)} - v^s_{y(i-1,j)})}{dy}$$

$$= -\frac{1}{K^\varphi_{(i,j)}(1 - \varphi_{(i,j)})}$$

$$\left(\frac{(p^t_{(i,j)} - p^{t0}_{(i,j)})}{dt} - \frac{(p^f_{(i,j)} - p^{f0}_{(i,j)})}{dt}\right) - \frac{p^t_{(i,j)} - p^f_{(i,j)}}{\eta^\varphi_{(i,j)}(1 - \varphi_{(i,j)})}$$

(35)

$$\frac{(v^D_{x(i,j)} - v^D_{x(i,j-1)})}{dx} + \frac{(v^D_{y(i,j)} - v^D_{y(i-1,j)})}{dy}$$

$$= \frac{1}{K^\varphi_{(i,j)}(1 - \varphi_{(i,j)})}\left(\frac{(p^t_{(i,j)} - p^{t0}_{(i,j)})}{dt} - \frac{(p^f_{(i,j)} - p^{f0}_{(i,j)})}{dt}\right) + \frac{p^t_{(i,j)} - p^f_{(i,j)}}{\eta^\varphi_{(i,j)}(1 - \varphi_{(i,j)})}$$

(36)

Fig. 6a and b represent the stencils used to discretise the Darcy Eq. (12) for respectively *x*- any *y*-Darcy velocity components:

$$v^D_{x(i,j)} = -\frac{k_{(i,j)}}{\eta^f_{(i,j)}}\left(\frac{(p^f_{(i,j+1)} - p^f_{(i,j)})}{\Delta x} - \rho^f_{(i,j)}g_x\right)$$

(37)

$$v^D_{y(i,j)} = -\frac{k_{(i,j)}}{\eta^f_{(i,j)}}\left(\frac{(p^f_{(i+1,j)} - p^f_{(i,j)})}{\Delta y} - \rho^f_{(i,j)}g_y\right)$$

(38)

Porosity evolution is computed by rewriting Eq. (27) in a slightly modified way [Gerya, 2019]:

$$\frac{D^s \ln\left(\frac{1-\varphi}{\varphi}\right)}{Dt} = \frac{1}{K^\varphi(1 - \varphi)\varphi}\left(\frac{D^s p^t}{Dt} - \frac{D^f p^f}{Dt}\right) + \frac{p^t - p^f}{\eta^\varphi(1 - \varphi)\varphi}$$

(39)

simplifying the computation of the porosity change, which is discretised on Eulerian nodes as [Gerya, 2019]:

$$\Delta\varphi_{(i,j)} = \frac{(p^t_{(i,j)} - p^{t0}_{(i,j)} - p^f_{(i,j)} + p^{f0}_{(i,j)})}{K^\varphi_{(i,j)}(1 - \varphi_{(i,j)})\varphi_{(i,j)}dt} + \frac{(p^t_{(i,j)} - p^f_{(i,j)})}{\eta^\varphi_{(i,j)}(1 - \varphi_{(i,j)})\varphi_{(i,j)}}$$

(40)

with

$$\Delta\varphi_{(i,j)} = \frac{D^s \ln\left(\frac{1 - \varphi_{(i,j)}}{\varphi_{(i,j)}}\right)}{Dt}$$

(41)

The logarithmic term ensures that porosity values always stay between 0 and 1. Subsequently, nodal porosity change $\Delta\varphi$ is interpolated on Lagrangian markers (see next section) and new porosity can be
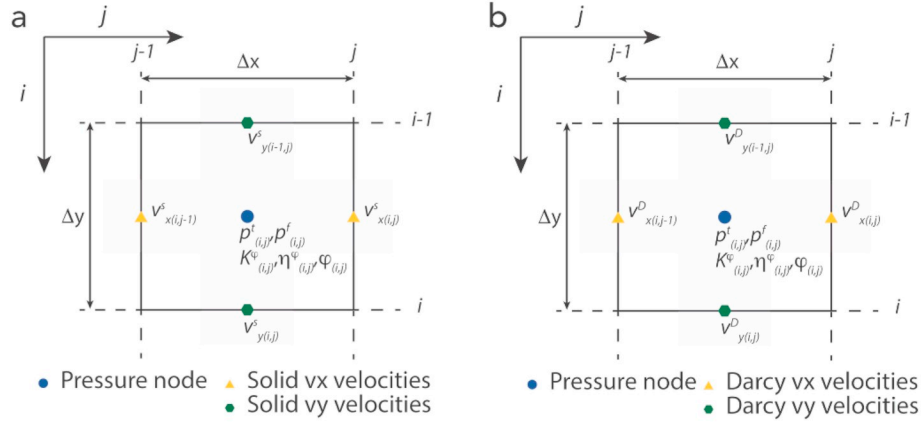
Fig. 5. Stencils for discretising the mass conservation equations. a) for solid matrix (Eq. (13)) and b) for fluid (Eq. (14)).

computed on markers [Gerya, 2019] (see appendix for full derivation):

$$\varphi_{new}^m = \frac{\varphi^m}{(1 - \varphi^m)e^{(\Delta\varphi^m dt)} + \varphi^m} \tag{42}$$

where φ^m is porosity on markers and $\Delta\varphi^m$ the interpolated porosity change.

2.4.1. Interpolation of Material Properties between Markers and Nodes

To transport material properties and to accurately treat $\frac{D^s}{Dt}$ and $\frac{D^f}{Dt}$, Lagrangian markers are distributed randomly throughout the entire Eulerian grid. The markers are then advected in accordance with computed solid matrix velocity field [Gerya, 2019]. The interpolation of any parameter B from markers to surrounding nodes is done by a distance dependent weighted average (Fig. 7):

$$B_{(i,j)} = \frac{\sum_m B^m w_{(i,j)}^m}{\sum_m w_{(i,j)}^m} \tag{43}$$

$$w_{(i,j)}^m = \left(1 - \frac{\Delta x^m}{\Delta x}\right)\left(1 - \frac{\Delta y^m}{\Delta y}\right) \tag{44}$$

where $B_{(i,j)}$ and B^m are respectively nodal and marker values of the parameter B, Δx^m and Δy^m are the distance from marker to node.

To account for nodal property changes related to advection of deviatoric stresses and solid matrix velocity components we used an incremental marker-based scheme proposed by Herrendörfer et al. [2018]. This advection scheme is suitable for small marker
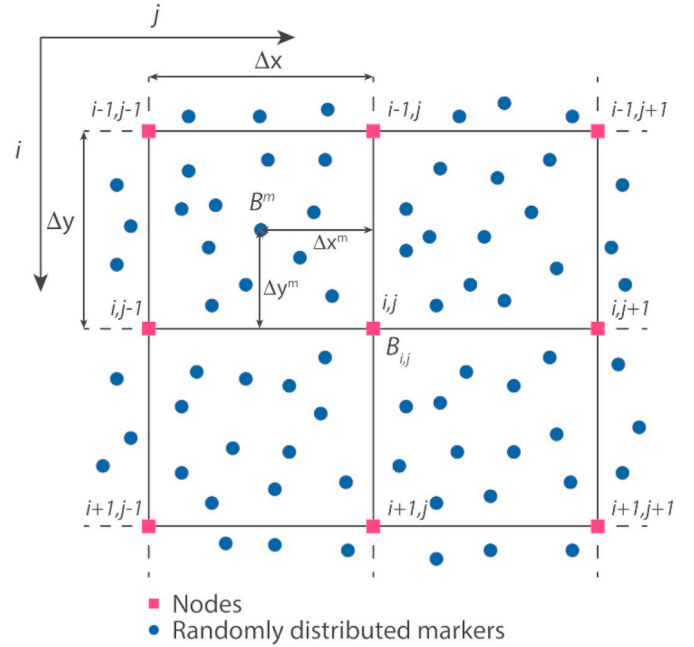
Fig. 7. Interpolation stencil of material properties from markers to nodes. B^m is the m-th marker carrying the material property B and $B_{(i,j)}$ is the i,j-th node to which the material property B is interpolated.
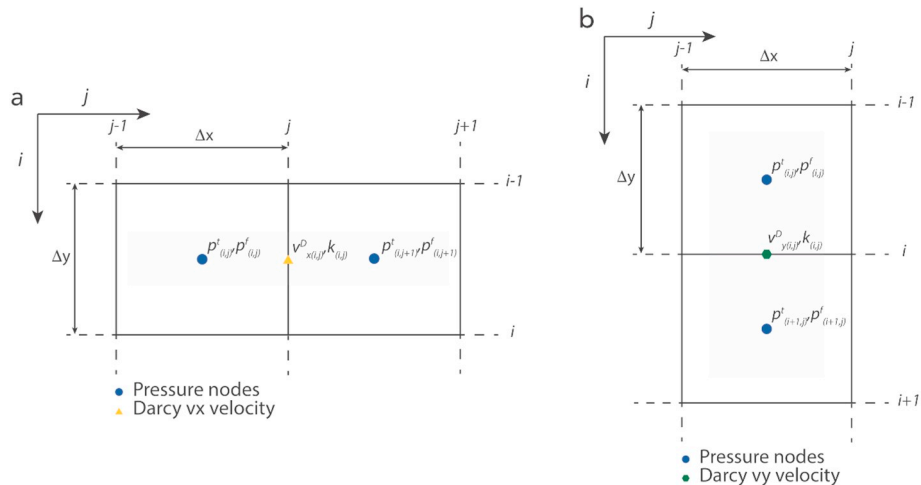

Fig. 6. Stencils for discretising the Darcy equations. a) x-Darcy equation (Eq. (12)) and b) y-Darcy equation (Eq. (12)).

displacements used in our experiments. This approach interpolates the advected quantity B from nodes to markers before the advection as (Fig. 7):

$$B^m = w_{(i,j)}^m B_{(i,j)} + w_{(i-1,j)}^m B_{(i-1,j)} + w_{(i,j-1)}^m B_{(i,j-1)} + w_{(i-1,j-1)}^m B_{(i-1,j-1)} \tag{45}$$

where the indexes i,j indicate the nodal indexes around the cell were the marker is located. Once the new quantity is interpolated to the markers, it is re-interpolated back to the nodes to define the "non-advected" quantity (B^n) on the Eulerian grid. A 4-th Runge-Kutta scheme is then used to advect each marker to its new position according to the velocity field. During this advection step the stresses are rotated according to the vorticity field. The new advected quantity (B^a) is then re-interpolated from markers to nodes. The "non-advected" quantity is finally subtracted from the "advected" one giving an advection-related quantity increment ΔB for the Eulerian nodes caused by advection. The nodal quantity B is then updated for advection as:

$$B = B + \Delta B \tag{46}$$

A semi-Lagrangian method (or back-tracing method) [Gerya, 2019] is used to compute the nodal values of solid and fluid pressure advected respectively along solid and fluid velocity fields (i.e. by tracing the positions of Lagrangian points overlapping with Eulerian pressure nodes back in time to their departure point, where the advected values of fluid and total pressure are obtained by interpolation). The fluid velocity for this advection is computed as:

$$v^f = \frac{v^D}{\varphi} + v^s \tag{47}$$

2.5. SHM model setup

The above described numerical model was applied to a simplified 2D subduction zone setup (Fig. 8), based mainly on the setup used by [van Dinther et al., 2013a]. The studied domain has a size of 150×64 km and a spatial resolution of 1 km in both x and y direction. An inclined gravity field is used [van Dinther et al., 2013a] that corresponds to a slab dipping at 20°. The slab and the forearc of constant high viscosity are separated by a lower-viscosity subduction channel for which typical effective viscosity values for subduction interface, in agreement with values derived from experimentally calibrated flow laws, are used [e.g., Duretz et al., 2012; Gerya et al., 2002; Ranalli, 1995; van Dinther et al., 2013b]. The brittle-ductile transition region in the subduction channel is simulated by matrix shear viscosity gradually

Table 1
Model parameters.

Parameters	Values			
	Subduction channel	Forearc and plate	Water	Units
Rock density	3000	3000	1000	Kg/m^3
Rock shear viscosity	$1 \cdot 10^{21}$	$1 \cdot 10^{23}$	$1 \cdot 10^{-3}$	Pa·s
Porosity	1	1	1	%
Reference porosity	1	1	1	%
Critical porosity	20	20	20	%
Reference permeability	$1 \cdot 10^{-19}$	$1 \cdot 10^{-19}$	$1 \cdot 10^{-15}$	m^2
Shear modulus	$2.5 \cdot 10^{10}$	$2.5 \cdot 10^{10}$	$2.5 \cdot 10^{10}$	Pa
Cohesion	$3 \cdot 10^6$	$3 \cdot 10^8$	$3 \cdot 10^6$	Pa
Confined friction coefficient	0.3	0.3	0.3	–
Tensile friction coefficient	1	1	1	–
Fluid density	1000	1000	1000	Kg/m^3
Fluid viscosity	$1 \cdot 10^{-3}$	$1 \cdot 10^{-3}$	$1 \cdot 10^{-3}$	Pa·s
Plate fluid flux			$-1 \cdot 10^{-12}$	m/s
Convergence rate			1.6	cm/yr

decreasing downwards mimicking the temperature increase, as in [van Dinther et al., 2013b] (Cf. colour gradient in Fig. 8). Above this transition the sufficiently high channel viscosity ($1 \cdot 10^{21}$ Pa·s) guaranties its purely elasto-plastic behaviour, with only negligible viscous deformation. We use high permeability and low viscosity sticky water layer (see Fig. 8 and Table 1) to approximate the free surface condition [Crameri et al., 2012; Gerya, 2019; Schmeling et al., 2008] on the top of the overriding plate. Due to its very low viscosity this layer always behaves purely viscously and does not accumulate any elastic stresses. At the bottom of the computational domain, a constant subducting slab velocity is applied simulating subduction of the slab. The basal fluid flux approximates slab dehydration. Physical properties used for different materials are specified in Table 1. Throughout the domain, to approximate small properties heterogeneities, an initial random porosity distribution is assumed such that:

$$\varphi = \varphi_{init} (1 + 0.5(rand - 0.5)) \tag{48}$$

where $rand$ is a function giving a random number between 0 and 1 and φ_{init} a constant background value. This leads to random variations in shear modulus, viscosity and compressive and tensile strength of rock markers due to Eqs. (7), (9)–(11) and (28)–(32).

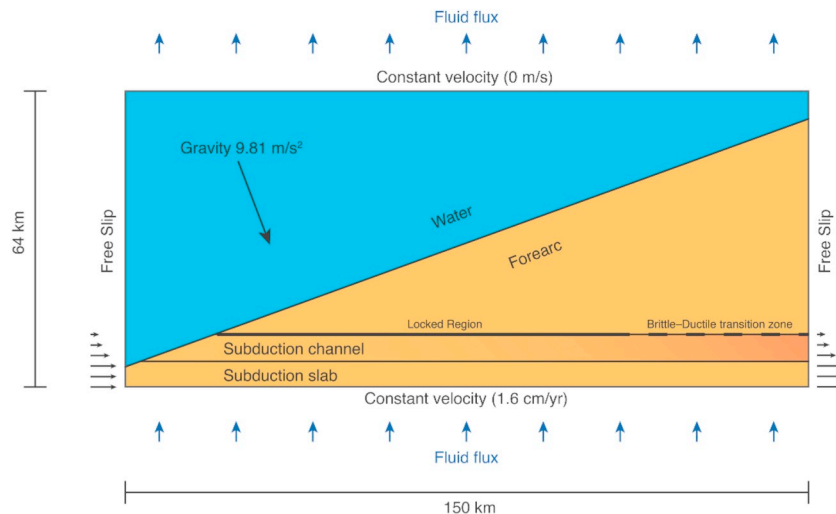Given the methodological nature of this paper, the investigated

Fig. 8. Sketch showing the simplified 2D subduction setup used in numerical experiments. A brittle-ductile transition is introduced by gradually reducing viscosity (shown by the colour gradient in the subduction channel), as is expected to occur with increasing temperatures [van Dinther et al., 2013b]. Figure not in scale.

SHM subduction model is chosen to be rather simple and its parameter space was not fully explored.

3. Results

This section describes results from numerical experiments on the simplified seismo-hydromechanical subduction system. First, based on our reference model, we demonstrate an intrinsic seismicity of this system and show the potential of our model for the investigation of a broad spectrum of transient slip phenomena. Then, we investigate the physics and mechanics of earthquakes in our model and discuss characteristic stages of a typical fluid-assisted seismic event. Finally, to some extent we investigate the model parameter space. We show that in our experiments the effective large-scale and long-term permeability of rocks in subduction zone is a key parameter to define spatio-temporal fluid pressure distribution during subduction, controlling transition from predominantly seismic to predominantly aseismic slip along the subduction interface.

3.1. How solid-fluid coupling generates earthquakes

The SHM numerical tool produces spontaneous highly localized (in both space and time) seismic events at the subduction interface (Figs. 9 and 10). Fig. 9 shows a megathrust event that nucleated in the downdip part of the domain (Fig. 9b) and propagating upwards with a slip rate on the order m/s.

To understand the physics of a seismic event, different parameters were monitored and analysed along the fault forming inside the subduction channel. This reveals how compaction, deformation and fluid flux play a crucial role in dynamically weakening and strengthening the interface between the subducting and overriding plate during rupture propagation.

To understand the evolution of one seismic cycle we characterize four main different stages with different dominant deformation characteristics within this cycle: (1) tectonic loading (i.e. interseismic period), (2) rupture nucleation, (3) rupture propagation, (4) rupture arrest and post-seismic relaxation (i.e. postseismic period).

During the interseismic period, inelastic deformation predominantly occurs in the deep part of the subduction interface, where viscosity is low. Below the locked seismogenic zone fluid pressure nearly equals the lithostatic one (Fig. 10 and 11d) due to viscous compaction of the weak creeping rock matrix under tectonic loading (Fig. 11c). Because of the relative low viscosity of the matrix, tectonic loading induces a broadly distributed deformation and viscous pore compaction occurs in this zone under conditions of low deviatoric stresses thereby creating a
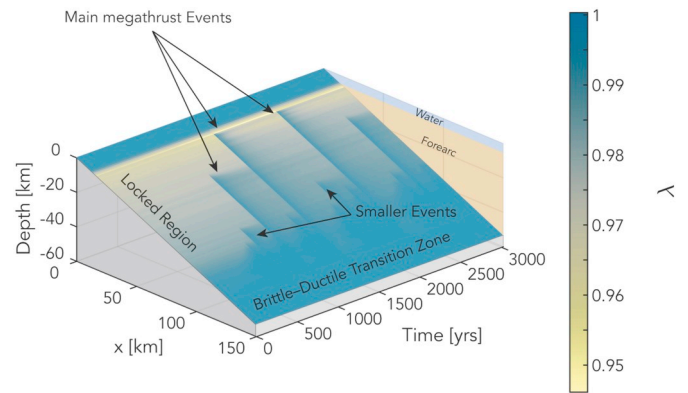

Fig. 10. Spatiotemporal evolution of the pore fluid pressure ratio ($\lambda = p^f/p^t$). Downdip, in the brittle-ductile transition, fluid pressure is always close to lithostatic, whereas during events high fluid pressure can extend through the locked region resulting in a high pore fluid pressure ratio for the event duration and sometime afterwards.

uniform (i.e. non-localized) fluid pressurization (Fig. 11a, b). However, more updip viscous compaction becomes less efficient, as the transition from ductile to brittle/plastic deformation occurs due to the prescribed gradual increase in subduction channel viscosity as inspired by a temperature decrease [e.g., van Dinther et al., 2013b]. A decrease in viscous compaction creates more favourable conditions for localized faulting. In addition, going more updip into the locked zone the viscosity increase causes a gradual increase in deviatoric stresses along the interface, which brings it closer to brittle/plastic failure. Furthermore, the visco-elastic stress build-up is emphasized by differential displacement as the updip region is locked, while subduction and tectonic loading cause ductile creep in the low-viscosity region of the subduction channel (Fig. 11a). Stress build up continues until a critical stress and fluid pressure are reached over a large enough area.

The second stage of fluid-induced seismic events involves the nucleation of a spontaneous rupture (Fig. 12). The high fluid to total pressure ratio $\lambda = p^f/p^t \approx 1$ (Fig. 12d) lowers the brittle/plastic strength of the rock (Eq. (22)) inducing spontaneous localisation of a slowly creeping brittle/plastic fault that gradually lengthens in the updip direction, with $\sigma_{II}' = \sigma_{yield}$. The resulting local stress drop during the event induces a stress increase ahead of the rupture front to conserve momentum [e.g., van Dinther et al., 2013a]. This local stress increase at the tip of the propagating rupture, with help of the high pore fluid to total pressure ratio, will trigger brittle/plastic deformation
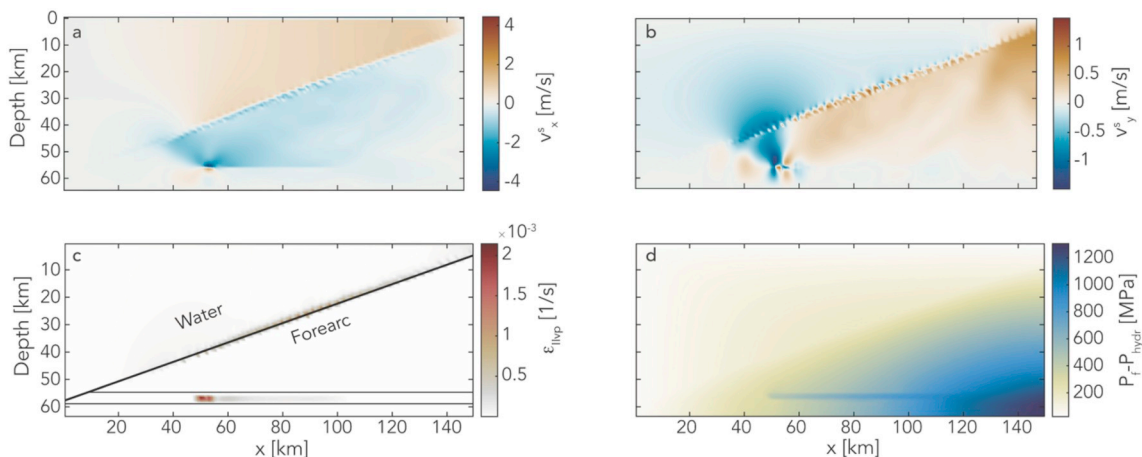

Fig. 9. Snapshot of fluid-induced megathrust earthquake. a) solid x velocity field, b) solid y velocity field, c) square root of viscoplastic strain rate second invariant showing the highly localized fracture forming during an event, d) Pore fluid pressure without the hydrostatic component, showing the high fluid pressure present inside the fault propagating together with the rupture. Snapshot of event in model with $k^0 = 6 \cdot 10^{-19}$ m^2 and convergence rate of $2 \cdot 10^{-9}$ m/s.
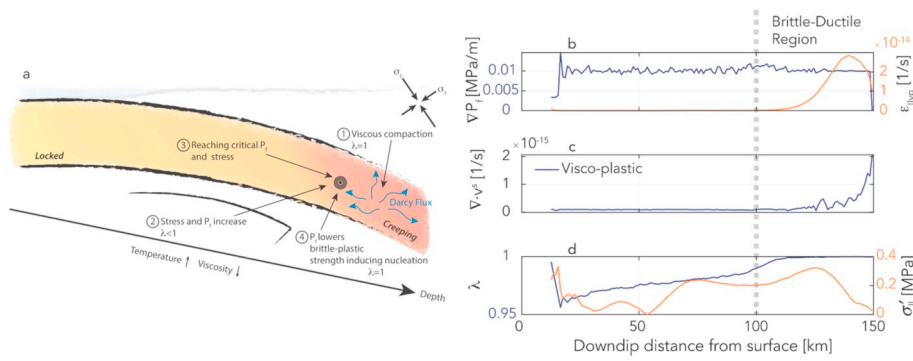
Fig. 11. First stage of fluid induced seismic cycle, event nucleation. a) Sketch with blown up subduction channel representing the build-up of fluid pressure and stress in the brittle-ductile transition zone, b) Fluid pressure gradient along the interface (blue line), being constant at the beginning and square root of visco-plastic strain rate second invariant (orange line), c) Compaction along the subduction interface, which is predominantly viscous at this early stage, d) fluid to total pressure ratio along the interface, indicating nearly lithostatic fluid pressure downdip to the brittle-ductile transition zone and square root of the second invariant of the deviatoric stress along the fault (orange line). (For interpretation of the references to colour in this figure legend, the reader is referred to the web version of this article.)

further updip, as in a hydro-mechanical runaway. The overall positive effective pressure (i.e. $p_e = p^t - p^f > 0$, Cf. Eq. (27)) inside the deforming fault causes its gradual visco-plastic compaction, which increases its pore fluid pressure. This pressurization causes progressive weakening of the growing fault that in turn accelerates its further brittle/plastic deformation, compaction and fluid pressurization. The positive dynamic weakening feedback inside the fault produces spontaneous transient slip (Fig. 12). It is remarkable that in the slip region total (i.e. visco-elasto-plastic) compaction is relatively small and does not change much (Fig. 12c). This is because the irreversible visco-plastic compaction under condition of $p^t > p^f$ (Cf. Eq. (27)) is associated with and almost fully compensated by reversible elastic decompaction caused by an increase in fluid pressure under condition of $D^s p^t / Dt < D^f p^f / Dt$ (Cf. Eq. (27)). As a result, the main effect of the deformation inside the fault is not a change in pore volume, but rather an increase in fluid pressure at the tip of the fault. This creates positive fluid pressure gradient in front of the rupture (Fig. 12b), which drives the fluid updip. This in turn increases $\lambda = p^f/p^t$ (Fig. 12d) and thus reduces the rock strength (Eq. (22)) in front of the rupture, thereby allowing its further updip propagation.

The slower slip event stops after ~1.7 days (Fig. 13) since the low accumulated deviatoric stresses further updip preclude further self-sustained propagation of the fault. Fig. 13 clearly suggests that slower and smaller (precursory) events nucleate (rather abruptly) in the low effective pressure region of the subduction interface, where fluid to total pressure ratio is high (Fig. 13c). Since this slower slip event happens entirely in a high fluid pressure region, where the rock strength is very low and small elastic energy release results in a relatively slow motion (Fig. 13a), a relatively moderate (< 0.014 MPa/m) fluid pressure gradient is produced in front of the fault during the event (Fig. 12b, Fig. 13b).

The subsequent precursory slower slip events are responsible for the progressive lengthening of the weakened (i.e. high $\lambda = p^f/p^t$) zone in the updip direction inside the subduction interface (Fig. 10). Furthermore, during such events, the accumulated elastic energy is not fully

released (Fig. 18a), thereby causing the entire subduction interface to finally approach its critical stress/strength state that is typical behaviour during the super-cycle [e.g., Herrendörfer et al., 2015]. Once enough elastic strain energy and stress have been accumulated and a critical fluid pressure is reached at the brittle-ductile transition zone, a large event is able to nucleate (Figs. 10, 15 and 16). Growing fluid pressure caused by the visco-plastic compaction inside the fault drives again an updip fluid flux causing fluid pressure increase and strength decrease in front of the fault (Fig. 15b and 16b). Due to the critical state of the subduction interface in front of the propagating fault it keeps its self-accelerating lengthening: the faster is the deformation of the fault the faster is its visco-plastic compaction and fluid pressurization that causes updip fluid injection in front of the fault (cf. Figs. 12b-c and 15b-c). This feedback allows acceleration of the fracture to seismic speed (Fig. 16a) releasing a major part of the accumulated elastic energy (Fig. 18b). The λ value along the fracture increases to 1 with propagating of the fault, showing a fully unlocked interface between the subducting plate and forearc (Fig. 10, 15d and 16c).

Similarly to the precursory events, during the large megathrust rupture, no significant change in porosity is observed along the fault since its irreversible visco-plastic compaction is again associated with, and almost fully compensated by, reversible elastic decompaction of pores (Figs. 12c, 14 and 15c). The combination of these two interrelated processes results in almost no effective change in porosity (and thus permeability, Eq. (28)) during the event. This event however leaves behind an increased fluid pressure zone caused by the viscoplastic compaction and strongly elastically stressed pores due to the elastic decompaction.

Once the entire accumulated elastic strain energy is released, rupture propagation stops (Fig. 17a). After major as well as precursory events, in the postseismic phase fluid pressure relaxes gradually with time due to an elastic compaction of stressed pores inside the fault that causes a fluid flux exiting the fault (Fig. 14). This creates a tendency for porosity reduction (compaction) in the seismically active subduction interface on a long-term (i.e. through many seismic cycles). Fluid flux
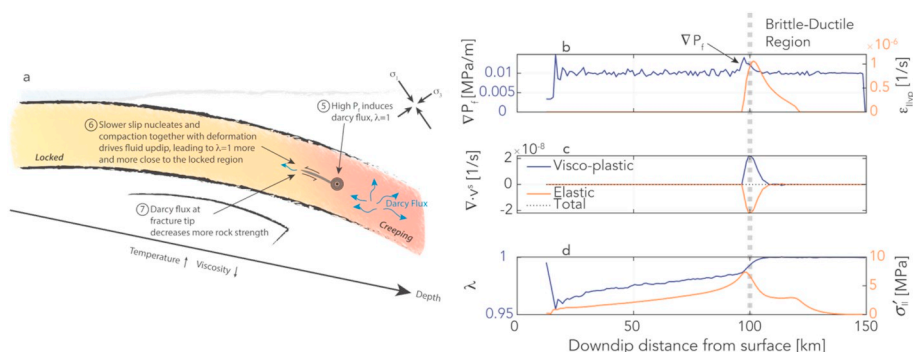

Fig. 12. Second stage of fluid induced seismic cycle, slower slip event propagation. a) schematic representation of slower slip event mechanism, b) Deformation (orange line) induced moderate (< 0.014 MPa/m) pore fluid pressure gradient (blue line) at the tip of the propagating fault, c) Compaction along the fault during major event, showing no significant pore volume change, d) increasing λ parameter along the propagating fault with increasing stress at the tip of the propagating fracture (orange line). (For interpretation of the references to colour in this figure legend, the reader is referred to the web version of this article.)
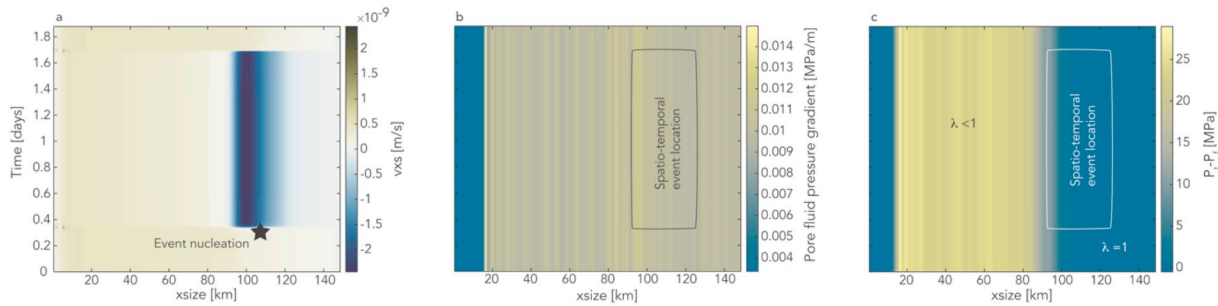
Fig. 13. Spatiotemporal evolution of a slower slip event propagation. a) Slip velocity in x direction with nucleation spot (black star), b) Relatively moderate (< 0.014 MPa/m) fluid pressure gradient is visible at the tip of the fault during a smaller and slower event, in contrast to a larger and faster event (cf. pressure gradient scale in Fig. 16b), c) Effective pressure that is low downdip ($\lambda \approx 1$) but remains high updip in the locked region ($\lambda < 1$).

and fluid pressure diffusion through the matrix, driven by the localized high pressure inside the fault, allow the fluid pressure in the inactive fault plane to decrease leading the subduction interface to recover gradually its higher strength at lowered fluid/total pressure ratio ($\lambda < 1$) (Fig. 10 and 17d). The interface becomes gradually more and more stressed (Fig. 17d) and stress build up and a super-cycle can re-start [Herrendörfer et al., 2015] mainly on the same fault plane weakened by the high fluid pressure induced by previous events as this fluid pressure anomaly is not fully relaxed during the interseismic deformation. New ruptures are more likely to occur where rock strength is lower and less stress is needed to fracture the rock, i.e. where the rock strength is weak because of the high fluid pressure left by the previous seismic events. Elastic stress accumulation and visco-plastic deformation starts again in the downdip part of the subduction interface close to the brittle ductile transition region (Fig. 17b, c, Fig. 10).

3.2. Earthquake cycle

Our numerical experiments showed that the fully coupled poro-visco-elasto-plastic hydro-mechanical subduction system shows intrinsic seismic properties. Our reference numerical model shown in Fig. 18 shows quasi-periodic seismic events ranging from slower transient events to regular earthquakes that exhibit slip velocities of m/s (Fig. 18, (b)). Earthquake nucleation in our SHM system arises spontaneously from spatio-temporal variations in effective pressure coupled to local variations of the brittle/plastic strength of fluid-bearing rocks. This rheological coupling can thus generate both weakening and strengthening of rocks thereby inducing a dynamic behaviour characteristic for rate- or rate- and state-dependent friction without

including that explicitly.

In our reference model, the different events nucleate downdip around the brittle-ductile transition and propagate predominantly updip (see previous section) showing eventually the capability of the larger events to rupture all the way up to the trench. Different size events are organized in form of a super-cycle [e.g., Herrendörfer et al., 2015] in which several partial ruptures culminate with a large event (Fig. 18) propagating along the entire subduction interface (Fig. 10). Fig. 18 (a) shows the square root of the stress second invariant accumulation and drop during the seismic cycle in the model. Largest stress drops of a few MPa are indeed characteristic for the major full interface ruptures, whereas during slower partial ruptures the stress drop stays way below one MPa (Fig. 18, c). Maximal slip velocity and stress drop during the events seem to be positively correlated (Fig. 18c). Fig. 18 (d) displays an attempt to classify the modelled earthquakes into slow and regular according to their duration and moment magnitude computed according to Blaser et al. [2010]. We defined the duration of an event from the start of yielding to its complete end and the fault width, to scale empirically to the moment magnitude, was defined to be the maximum yield width during an event. Faster events lie well on the scaling line for regular earthquakes defined by Ide et al. [2007] (Fig. 18d). Slower events show a different trend than regular earthquakes, with some of them lying on the slow earthquake scaling line, some of them also on the earthquake scaling and other in between (Fig. 18d).

3.3. Permeability influence on seismic behaviour

Permeability is the principal parameter affecting fluid transport in a
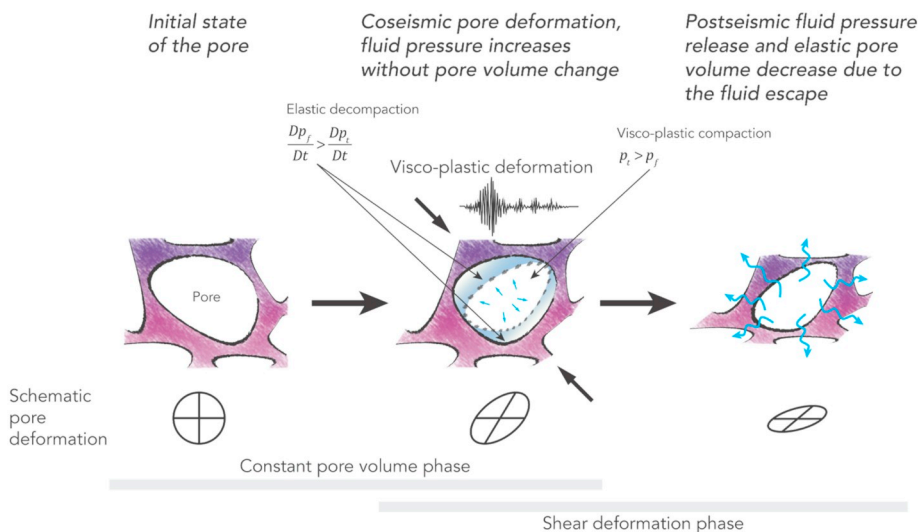

Fig. 14. Schematic pore and matrix deformation during pre-, co- and postseismic stages. During coseismic deformation fluid pressure increases without any significant pore volume change. On low permeability conditions Darcy velocity is close to zero (see Eq. (12)), leading to a close to zero Darcy velocity divergence (Eq. (14)), this results in elastic decompaction compensating for visco-plastic compaction during the coseismic stage.
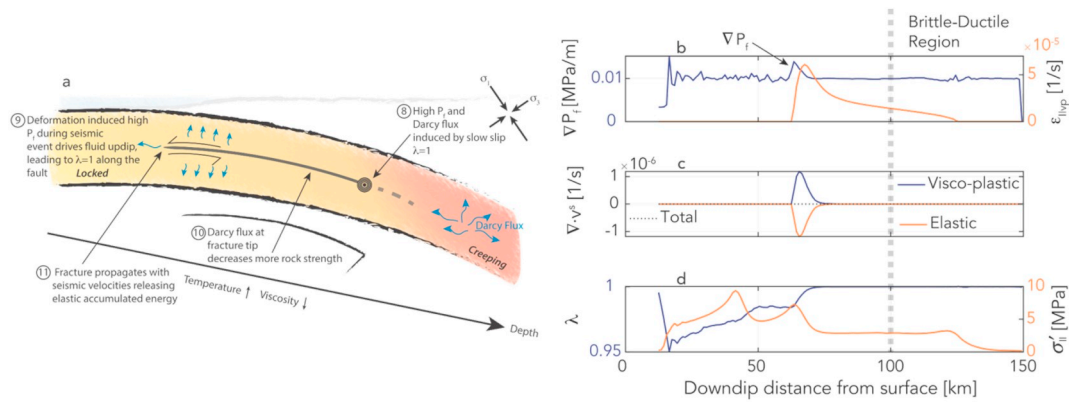
Fig. 15. Third stage of fluid induced seismic cycle, megathrust earthquake propagation. a) schematic representation of megathrust event mechanism, b) Deformation (orange line) induced high (> 0.02 MPa/m) pore fluid pressure gradient (blue line) at the tip of the propagating fault, c) Compaction along the fault during major event, showing no significant pore volume change, d) increasing λ parameter as well as stress (orange line) along the propagating fault. (For interpretation of the references to colour in this figure legend, the reader is referred to the web version of this article.)

porous matrix [e.g., McKenzie, 1984], being a crucial parameter determining how fluid pressure can vary during subduction [e.g., Dymkova and Gerya, 2013]. It should be noted that in our simplified SHM model a large-scale and long-term effective permeability of rocks is considered that only depends on porosity (Eq. (28)) and neglects effects of rock fracturing that may cause highly localized fluid fluxes.

To investigate to some extent the parameter space of our subduction model we performed a set of numerical experiments by changing both the permeability and the plate convergence rate (Fig. 19). Generally, models with lower permeability showed reduced maximal slip velocity and predominant aseismic slip along the subduction interface (Fig. 19a), whereas higher permeability models showed increased maximal slip velocities and predominant seismic slip. Lower permeability also resulted in increased fluid/total pressure ratios λ along the interface that varied insignificantly with time whereas higher permeability produced lowered ratios that increased strongly only during major seismic events (Fig. 19b). The effect of convergence velocity changes for both the slip character and the λ values was much less pronounced (Fig. 19).

Lower permeability, and the ensuing suppressed fluid flow, results in precluding significant both spatial and temporal effective pressure (and thus λ values and rock strength) variations inside the model. This causes fluid pressure to be always very close or equal to total pressure (locking degree very low, i.e. low resistance to slip (Fig. 19b)), making it easy to yield given the little elastic stress accumulation needed to reach yielding. In contrast, higher permeability causes large spatial-temporal effective pressure (and thus λ values and rock strength) variations (Fig. 10) thereby creating favourable conditions for the seismic behaviour of the model (Fig. 19) controlled by coseismic effective pressure increase and its post- and interseismic relaxation (Fig. 14).

Different slip behaviour related to permeability can be also clearly seen by looking at the stress drop during the earthquake cycle (Fig. 20). Lower permeability models show nearly constant λ ≈ 1 value over the entire subduction interface, producing mostly stable sliding with some slower slip events characterised by small stress drop (Fig. 20). In contrast, higher permeability models show strongly spatially and temporally variable λ values along the propagating faults and super-cycle behaviour with slower slip events, regular earthquakes (partial ruptures) and full megathrust ruptures characterised by the largest stress drop (Fig. 20).

A relatively small decrease of less of an order of magnitude in the permeability (from 10^{-19} to $6{\cdot}10^{-20}$ m^2) causes a remarkable transition from large events dominated earthquake super-cycle (Fig. 18) to a slower-slip dominated simple cycle, where events are smaller but much more regular, similarly, to stick slip. Further reduction of permeability (to $5{\cdot}10^{-20}$–$3{\cdot}10^{-20}$ m^2) causes a transition to dominant aseismic stable slip behaviour. As is it can be seen in Fig. 20, convergence rate influence for the stress drop is again rather insignificant. It can be seen, however, that convergence rate has influence on the frequency of the events (Fig. 20). This emphasises that both the slip mode and stress drop magnitude in our simplified models are mainly controlled by the permeability rather than by the loading rate.

4. Discussion

4.1. Poro-visco-elasto-plastic rheological coupling

The model presented here contributes to a better understanding of the role of fluids in earthquake physics and mechanics and presents a possible self-consistent poro-visco-elasto-plastic mechanism of the
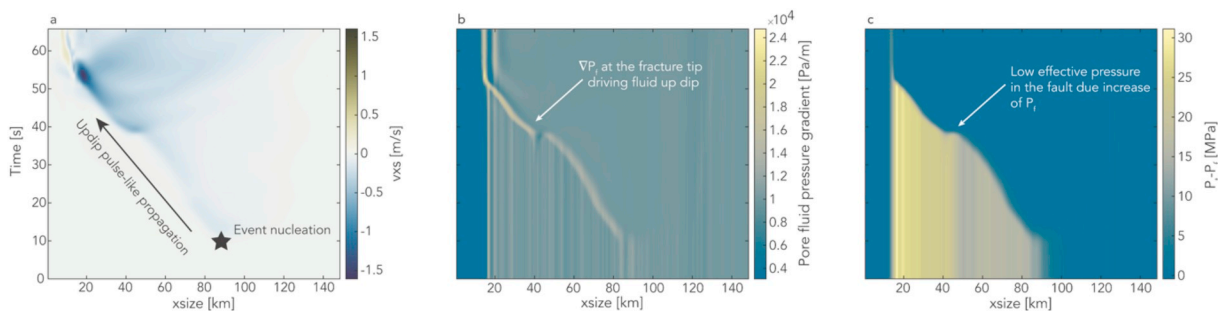

Fig. 16. Spatiotemporal evolution of a major megathrust event. a) Pulse-like rupture propagation with speed in the order of m/s, b) High fluid pressure gradient (> 0.02 Pa/m) propagation in front of the grooving fault, c) Effective pressure of the subduction interface decreasing with propagation of the fracture and the consequent increase in fluid pressure.
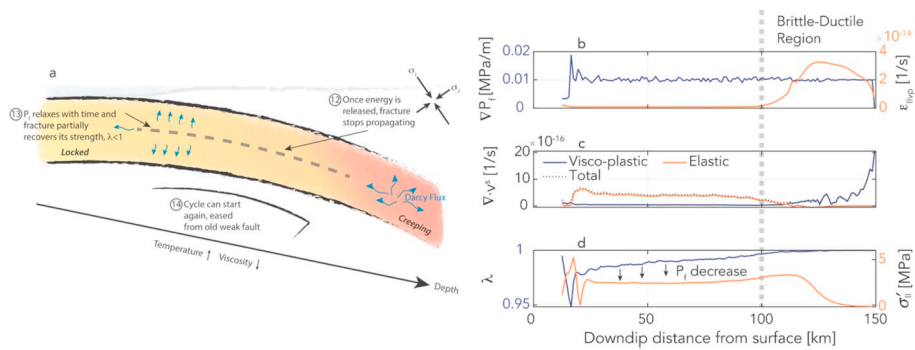
Fig. 17. Last stage of fluid induced seismic cycle, rupture arrest and post-seismic relaxation. a) Schematic representation of the relaxations stage and fault strength recovery, b) Fluid pressure gradient along the subduction interface (blue line) and downdip deformation (orange line), c) Elastic compaction preparing conditions for the nucleation of new events, d) Recovery (i.e. lowering) of fluid to total pressure ratio along the subduction interface leading to rock strength recovery (i.e. increase) after an event and square root of the second deviatoric stress invariant (orange line). (For interpretation of the references to colour in this figure legend, the reader is referred to the web version of this article.)

subduction interface strengthening and weakening acting during the earthquake cycle.

This mechanism can be either complementary or substitutional to common empirical rate- (and state-) dependent frictional laws used for seismic cycle and subduction seismicity modelling [e.g., Dieterich, 1979; Herrendörfer et al., 2018; Lapusta et al., 2000; Ruina, 1983]. The documented rheological coupling between the fluid flow and solid rock matrix deformation forces the system to behave intrinsically seismic without any addition of empirical rate- (and state-) dependent friction laws.

Seismic rupture always starts after reaching some significant initial/critical fault length during the aseismic fault growth (that always starts close to brittle-ductile transition). This type of behaviour is comparable to rate- and state-dependent friction models for propagating faults [e.g., Preuss et al., 2019], where a characteristic length-scale is present. From our model results we can infer that such critical weakening length always reaches the more locked and high viscosity region updip at approximately 100 km downdip. More research in this direction is needed, but this is beyond the scope of our study.

The numerical model shows that coseismic pressurization and related brittle/plastic weakening of the fault happens without substantial porosity or permeability change, whereas a long-term compaction is observed during interseismic periods being controlled by the poro-visco-elastic stress relaxation (Fig. 14). High fluid pressure in faults is typically thought to be one of the main reasons of their weakness and therefore to be one of the main potential causes of active seismicity along such faults [e.g., Lu et al., 2017; Rice, 1992; Sibson, 1990; Sleep and Blanpied, 1994]. This is the case when a transient increase of fluid pressure along the fault is caused by poro-elasto-plastic coupling. On the other hand, high fluid pressure caused by lowered permeability of rock shows a more stable slip behaviour (Fig. 20). Our poro-visco-

elasto-plastic model may thus potentially explain how spontaneous coseismic fault pressurization operates in nature due to the interplay between the visco-plastic compaction and elastic decompaction of pores (Fig. 14). From our results it is also evident that the intrinsic coupling of solid deformation and fluid flow plays a central role in subduction thrust seismicity.

4.2. Subduction seismicity spectrum

Fig. 18 shows a complete seismic cycle, with the presence of both regular and slower events, produced by our developed seismo-hydro-mechanical numerical tool. Fig. 18(d) attempts classification of these different events based on their characteristic duration and magnitude. For the faster events, it shows a clear match with the linear correlation found for ordinary earthquakes by Ide et al. [2007]. On the other hand, for the slower events, a clear departure from this correlation in the direction of slower seismic phenomena is observed, reflecting in some way what is seen in nature [Ide et al., 2007; Peng and Gomberg, 2010]. The classification of the modelled hydro-mechanical seismic events is yet preliminary since both the exact magnitude and duration of these events depend on the way of their detection in our SHM numerical models.

4.3. Model limitations

Already with a basic and simplified subduction setup, our new seismo-hydro-mechanical numerical tool shows ability to capture the broad subduction seismicity spectrum. In contrast to our simple model geometry, nature involves plenty of heterogeneities that influence seismic processes. In particular, fluid flux, porosity and permeability distributions along the subduction interface may be strongly
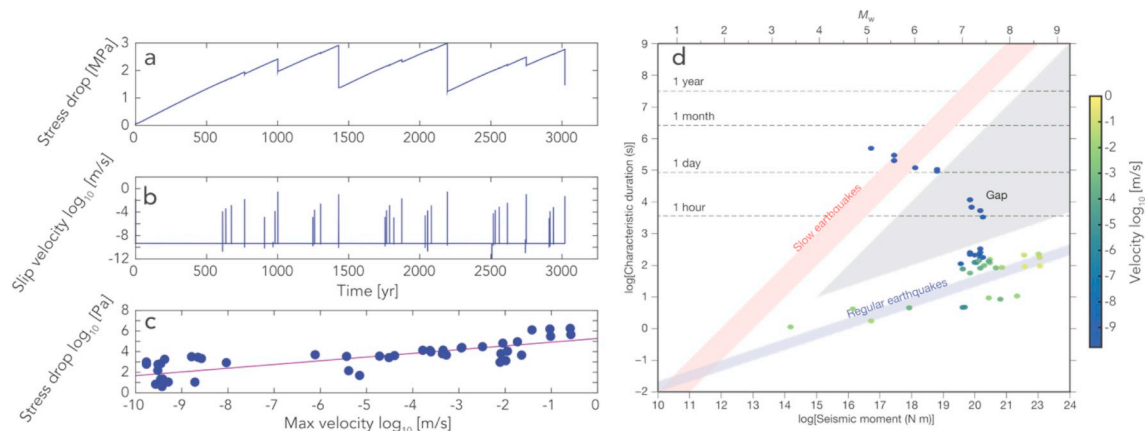

Fig. 18. Quasi periodic seismic cycle. a) Stress drop (σ_{II}') during the seismic cycle of a few MPa for the larger events, b) Seismic events modelled during a seismic cycle with megathrust events reaching velocity of the order of m/s and slower events (slip velocity is represented here by monitoring a point along the fault), c) Positive correlation between recorded maximal velocity of an event and its stress drop, no further statistical analysis was performed that is beyond the scope of this work, d) Classification of modelled events in regular and slow earthquakes by its duration and moment magnitude [modified after Ide et al., 2007].
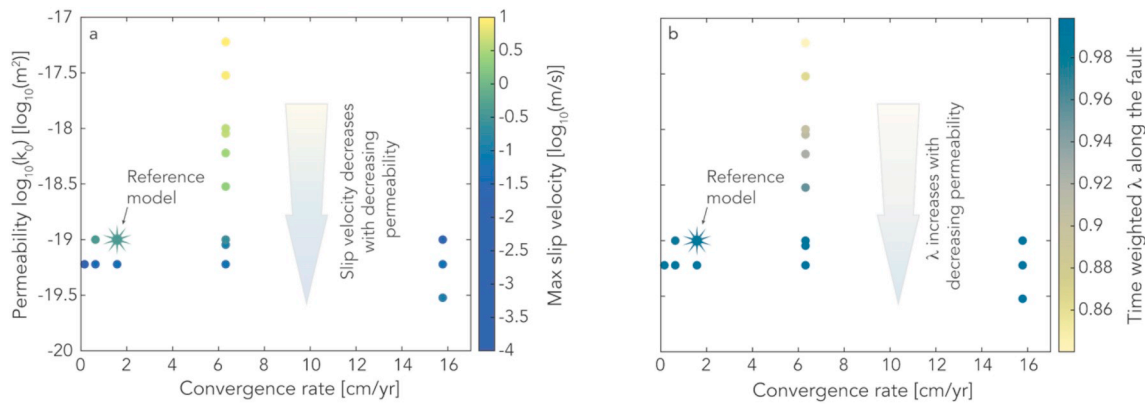
Fig. 19. Maximal slip velocity (a) and λ (b) relations to permeability and plate convergence rate.

heterogeneous, resulting potentially in a more complex seismic behaviour than the one documented in our models. Another important physical component missing in our simulations, is the influence of fractures on permeability of rocks [e.g., Coelho et al., 2015; Rutqvist et al., 2018]. Fractures can significantly affect both the coseismic fluid pressure build-up and its interseismic relaxation, thereby strongly affecting the seismic cycle. Higher permeability fractures can eventually drain fluid outside the subduction interface or in other locations, affecting the locking degree along the thrust and influencing in such way the nucleation, propagation, end and size of the different events. In contrast low permeability non-fractured regions may lead to faster increase of fluid pressure, low locking degree, in some regions affecting again the seismic behaviour in the subduction zone. It is also known that pre-existent faults, as well as their number, geometry and complex stress distributions can determine the type of seismic events as well influence their nucleation [Romanet et al., 2018]. Therefore, both fracture-controlled permeability mechanisms and pre-existing faulting patterns that are neglected here, should be included in future more comprehensive subduction seismicity models.

Furthermore, it is known that shear of a fluid-saturated granular material can cause dilatancy and a consequent pore pressure reduction [e.g., Brantut et al., 2018; Hamiel et al., 2005; Lockner and Stanchits, 2002; Segall and Rice, 1995]. However, this effect is poorly constrained at great depth and is only investigated experimentally at relatively low-pressure conditions [Brantut et al., 2018; Lockner and Stanchits, 2002; Segall and Rice, 1995]. It is likely that this effect will decrease with increasing confining pressure [e.g., Brantut et al., 2018] at larger

depths along the subduction interface close to the brittle ductile transition, where our events nucleate, and slow slip occurs. Furthermore, the dilatation is transient and is only characteristic for the initial stages of the slip (as porosity cannot increase indefinitely due to dilatation). As soon as enough strain is accumulated and the maximum dilatancy limit is reached, this effect will vanish. Therefore, in our study we focussed on exploring the fluid pressure related feedback between the elastic and visco-plastic (de)compaction of pores in a simplified manner. However, future research should also focus on the dilatancy effect, as well as the influence of rate- and state-dependent friction, also neglected in our study.

Parameters controlling shear zone thickness were not investigated in this study. The shear zone thickness will proportionally decrease with increasing model resolution, which is a characteristic behaviour of continuum-based plasticity models [e.g., Kaus, 2010; Templeton and Rice, 2008; Vermeer and de Borst, 1984]. However, the main messages in this paper and the key characteristics of the seismic cycle described are not affected. In particular, rupture velocity, maximal slip velocity, absolute maximal stress, total pressure, and fluid and effective pressure magnitudes during the rupture, as well as the critical weakening downdip depth reached aseismically before seismic rupture starts, remain relatively stable as well as the described characteristic seismic cycle behaviour (cf. Appendix A, Fig. A.1). There could potentially be some intrinsic shear zone finite width coming from elasto-viscoplastic compaction length scales that need to be investigated by future research.

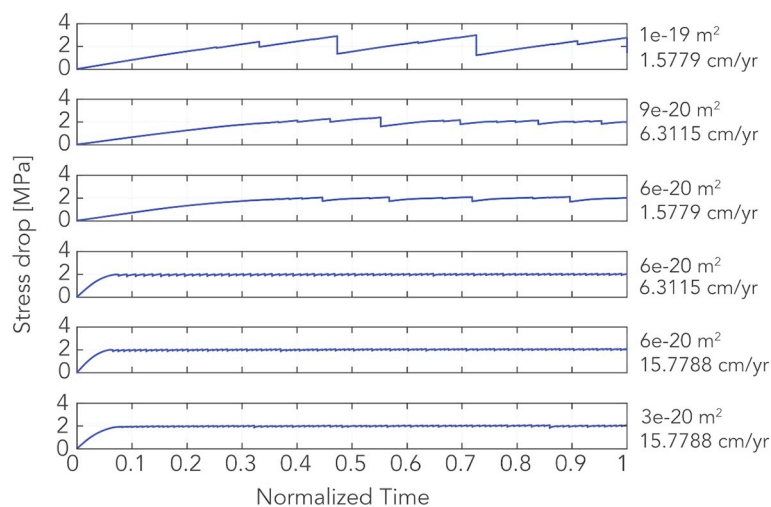Our model also neglects hydration/dehydration reactions

Fig. 20. Stress drop for different permeability and convergence rate. Time is normalized over the total simulation time, permeability and convergence rate are indicated on the right of every plot.
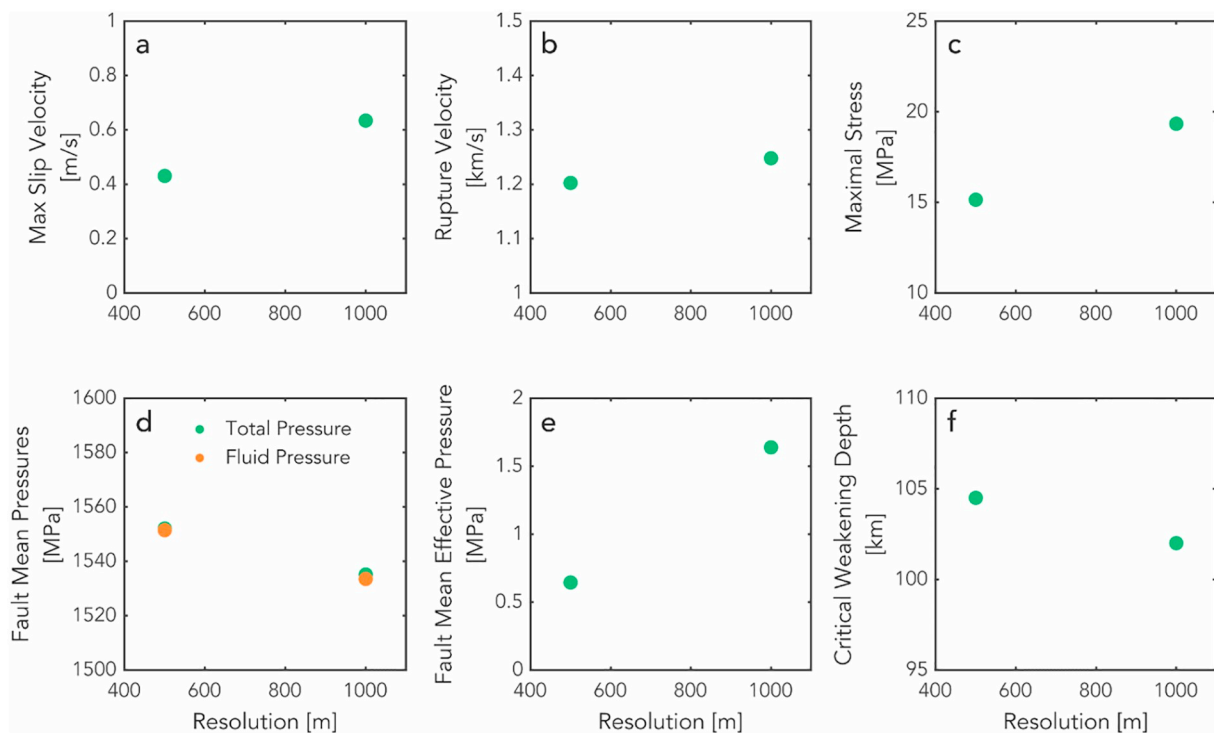
Fig. A.1. Model resolution test. a) Maximal slip velocity, b) rupture velocity, c) Maximal stress, d) total and fluid pressure, and e) effective pressure during rupture propagation and f) critical weakening downdip depth. The figure shows that the numerical solutions to our proposed methodology are only weakly dependent on grid size.

[Connolly, 1997], which can significantly influence pore volume as well as fluid flux. These important chemical processes should be taken into consideration when investigating more in details fluid fluxes in subduction zones and their implications for fluid pressure variations and weakening of the subduction interface.

An important simplification present in the described model is the highly simplified implementation of the influence of temperature on subduction interface properties. Temperature can in particular affect hydration/dehydration reactions in turn causing changes in fluid fraction (porosity), effective pressure and matrix rheology, which would eventually affect the way fluid pressure is build up or decreased inside the subduction interface including its brittle-ductile transition zone. Shear heating will increase fluid temperature expanding its volume and consequently increasing its pressure, leading to a further factor that could drive an instability along the subduction interface [Segall and Rice, 2006]. Therefore, including solution of energy conservation equation and exploring more realistic seismo-hydro-thermo-mechanical-chemical (SHTMC) subduction models will be required in the future.

Finally, a more complex non-Newtonian ductile matrix rheology is known to be also crucial for seismic behaviour, especially for the visco-elastic stress build-up and relaxation along the subduction interface during long-term deformation processes [e.g., KWang, 2007]. This makes a Newtonian ductile rheology assumption used in our models rather simplistic and calls for more realistic non-Newtonian flow law in the future implementations.

4.4. Outlook

The role of fluids in nucleation and propagation of seismic events is also known outside subduction thrust seismicity. It is widely known that fluids can trigger slower and also regular earthquakes in other geological settings such as volcanism or fluid injection when dealing with geothermal reservoirs, carbon sequestration or oil and gas recovery. Investigations in other setups and with other fluid properties

are necessary to understand those kinds of seismic events too and to asses if the mechanisms presented in this work hold also for other type of seismicity. Gaining knowledge on these different kinds of events would be of great significance for the entire society, improving risk assessment for induced events.

Something yet still poorly understood in a continuum medium, and that should be addresses in future works, is how porosity and/or permeability relate to each other's and evolves with the creation, propagation and dilation of fractures. Permeability-porosity relationships describe evolving of permeability with changing of solid matrix porosity based on theoretical assumption and/or measurements [e.g., Brantut et al., 2018; Carman, 1939; David et al., 1994; Gueguen and Dienes, 1989; McKenzie, 1984], however a full understand of their relationship is not yet present. Most equations, describing change in permeability related to either increase or decrease of porosity, are derived for homogeneous media, not fully considering grain shapes and heterogeneities [e.g., Bourbie, 1985; McKenzie, 1984]. Furthermore, little effort was made to understand and derive equations describing how porosity, and/or hence permeability, varies with brittle/plastic deformation in a two-phase system. Theoretical derivations have, however, been made for change in porosity due to plastic matrix deformation at a pore scale [Yarushina and Podladchikov, 2015], yet theoretical constitutive equations describing changes of porosity, and/or thus permeability, at a larger scale are still missing and need further investigation. The potential existence of a different permeability-porosity relationship or a permeability evolution with brittle/plastic deformation where fractures are created, will likely affect in a non-negligible way fluid transport in the subduction interface, influencing the seismic cycle and perhaps the physics driving those events as well.

Weakening of the rock play a crucial role in fracture and earthquake mechanics, thus another parameter that should be investigated is cohesion weakening and variation. Still now, not much is known about cohesion changes in function of other parameters. Something which is clear, is that cohesion decreases with increasing porosity [Wong and Baud, 2012; Yarushina and Podladchikov, 2015] (Eqs. (30) and (31))

and with accumulating plastic strain [Lavier et al., 2000]. However, if the given relationship describes the correct physics or if other parameters may also affect cohesion in an important manner has still to be further investigated.

Future work will be needed to understand more rigorously how different parameters affects the transition from stable sliding, to slow earthquake and to regular seismic events. It is also important to understand more deeply the interaction between slow slip events and regular earthquakes. In our experiments they are often connected into a super-cycle in which slower and smaller events are followed by large megathrust earthquakes (Fig. 19). Therefore, it is important to understand if also in nature slower events can prepare and/or trigger larger earthquakes.

5. Conclusions

Our seismo-hydro-mechanical numerical modelling study showed how and why fluid flow coupling with poro-visco-elasto-plastic rock deformation (Fig. 14) is crucial for modelling subduction thrust seismicity and for understanding the relationship of fluids with earthquakes and fault weakness evolution. Furthermore, it was shown that the fully coupled seismo-hydro-mechanical subduction model is able to produce a broad seismicity spectrum that includes both regular earthquakes and slower events bearing similarities with nature (Fig. 18d). It was also demonstrated that the long-term and large-scale solid matrix permeability of the subduction interface strongly controls its slip spectrum whereas the plate convergence rate predominantly affects the frequency of the produced events (Figs. 19 and 20). Last but not least, our numerical models also clarified the evolution through time of the locking degree of a subduction zone, in response to changes in fluid pressure in interseismic and coseismic periods (Fig. 10).

Declaration of Competing Interest

The authors declare that they have no known competing financial interests or personal relationships that could have appeared to influence the work reported in this paper.

Appendix A

A.1. Plastic multiplier

From Eq. (20) and the relationship between square roots of second invariants and their deviatoric components:

$$\sigma_{II} = \sqrt{\frac{1}{2}\sigma_{ij}'^2} \ \textbf{\textit{and}} \ \dot{\varepsilon}_{II} = \sqrt{\frac{1}{2}\dot{\varepsilon}_{ij}'^2} \tag{A.1}$$

it follows:

$$\dot{\varepsilon}_{II(plastic)} = \sqrt{\frac{1}{2}\left(\chi\frac{\sigma_{ij}'}{2\sigma_{II}}\right)^2} = \sqrt{\frac{1}{8}\frac{\sigma_{ij}'^2}{\sigma_{II}^2}\chi^2} = \frac{1}{2\sigma_{II}}\chi\sqrt{\frac{1}{2}\sigma_{ij}'^2} = \frac{1}{2}\chi \tag{A.2}$$

$$\chi = 2\dot{\varepsilon}_{II(plastic)} \tag{A.3}$$

A.2. Second invariants deviatoric stress–strain rate relationship

By inserting the following relationship

$$\sigma_{ij}' = 2\eta\dot{\varepsilon}_{ij}' \tag{A.4}$$

into the deviatoric stress relationship described in (A.1) and with some simple algebra one obtains Eq. (A.4) in terms of the square roots of second invariants:

$$\sigma_{II} = \sqrt{\frac{1}{2}(2\eta\dot{\varepsilon}_{ij}')^2} = \sqrt{4\eta^2\frac{1}{2}\dot{\varepsilon}_{ij}'^2} = 2\eta\sqrt{\frac{1}{2}\dot{\varepsilon}_{ij}'^2} = 2\eta\dot{\varepsilon}_{II} \tag{A.5}$$

A.3. Viscoplastic deviatoric strain rate and viscoplastic viscosity derivation

A viscosity-like definition for viscoplasticity can be derived starting from the sum of viscous and plastic deviatoric strain rates, following the relationship expressed in Eqs. (17), (18) and (20).

$$\dot{\varepsilon}_{ij(viscoplastic)}' = \dot{\varepsilon}_{ij(viscous)}' + \dot{\varepsilon}_{ij(plastic)}' \tag{A.6}$$

$$\dot{\varepsilon}_{ij(viscoplastic)}' = \frac{1}{2\eta}\sigma_{ij}' + \chi\frac{\sigma_{ij}'}{2\sigma_{II}} = \frac{1}{2}\sigma_{ij}'\left(\frac{1}{\eta} + \frac{\chi}{\sigma_{II}}\right) \tag{A.7}$$

By inserting Eq. (A.3) in (A.7) the viscoplastic deviatoric strain rate results in:

$$\dot{\varepsilon}_{ij(viscoplastic)}' = \frac{1}{2}\sigma_{ij}'\left(\frac{1}{\eta} + \frac{2\dot{\varepsilon}_{II(plastic)}}{\sigma_{II}}\right) = \frac{1}{2}\sigma_{ij}'\left(\frac{1}{\eta} + \frac{2\dot{\varepsilon}_{II(plastic)}}{\sigma_{II}}\right) \tag{A.8}$$

Using the relationship described in (A.5) is possible to rewrite the viscoplastic deviatoric strain rate as a function of the matrix shear viscosity and a plastic viscosity-like parameter:

$$\dot{\varepsilon}'_{ij(viscoplastic)} = \frac{1}{2}\sigma'_{ij}\left(\frac{1}{\eta} + \frac{1}{\eta^{pl}}\right)$$

(A.9)

with

$$\frac{1}{\eta^{pl}} = \frac{2\dot{\varepsilon}_{II(plastic)}}{\sigma_{II}} = \frac{\chi}{\sigma_{II}}$$

(A.10)

A viscoplastic viscosity-like parameter can then be defined as the sum of the matrix shear viscosity and the plastic viscosity-like parameter [Gerya, 2019]:

$$\frac{1}{\eta^{vp}} = \frac{1}{\eta} + \frac{1}{\eta^{pl}}$$

(A.11)

resulting, after some algebra, in:

$$\frac{1}{\eta^{vp}} = \frac{1}{\eta} + \frac{\chi}{\sigma_{II}} = \frac{\sigma_{II} + \chi\eta}{\eta\sigma_{II}}$$

(A.12)

$$\eta^{vp} = \eta\frac{\sigma_{II}}{\sigma_{II} + \chi\eta} = \eta\frac{\sigma_{II}}{\sigma_{II} + 2\dot{\varepsilon}_{II(plastic)}\eta}$$

(A.13)

A.4. Derivation of deviatoric visco-elasto-plastic stress

By discretizing in time the elastic deviatoric strain rate

$$\dot{\varepsilon}'_{ij} = \frac{1}{2G}\frac{D^s\sigma'_{ij}}{Dt} = \frac{1}{2G}\frac{\sigma'_{ij} - \sigma'^0_{ij}}{\Delta t}$$

(A.14)

where $\sigma'_{ij}{}^0$ is the deviatoric stress of the previous time step corrected for advection and rotation [Gerya, 2019], is possible to express the total deviatoric stress, in a viscosity-like manner, as a function of the total deviatoric strain rate (Eq. (17)):

$$\dot{\varepsilon}'_{ij} = \dot{\varepsilon}'_{ij(viscoplastic)} + \dot{\varepsilon}'_{ij(elastic)}$$

(A.15)

$$\dot{\varepsilon}'_{ij} = \frac{1}{2\eta^{vp}}\sigma'_{ij} + \frac{1}{2G}\frac{\sigma'_{ij} - \sigma'^0_{ij}}{\Delta t} = \sigma'_{ij}\left(\frac{1}{2\eta^{vp}} + \frac{1}{2G\Delta t}\right) + \sigma'^0_{ij}\frac{1}{2G\Delta t}$$

(A.16)

$$\sigma'_{ij} = \dot{\varepsilon}'_{ij}\left(\frac{2\eta^{vp}G\Delta t}{G\Delta t + \eta^{vp}}\right) + \sigma'^0_{ij}\left(\frac{1}{2G\Delta t}\frac{2\eta^{vp}G\Delta t}{G\Delta t + \eta^{vp}}\right) = 2\eta^{vp}\dot{\varepsilon}'_{ij}\left(\frac{G\Delta t}{G\Delta t + \eta^{vp}}\right) + \sigma'^0_{ij}\left(\frac{\eta^{vp}}{G\Delta t + \eta^{vp}}\right)$$

(A.17)

where $\dot{\varepsilon}'_{ij(viscoplastic)}$ is the deviatoric strain rate composed by viscous and plastic strain rate by means of the viscoplastic viscosity-like parameter η^{vp} defined in (A.13). The Eq. (A.17) can be easily rewritten in

$$\sigma'_{ij} = 2\eta^{vp}\dot{\varepsilon}'_{ij}Z + \sigma'^0_{ij}(1 - Z)$$

(A.18)

by setting

$$Z = \frac{G\Delta t}{G\Delta t + \eta^{vp}}$$

(A.19)

A.5. 2D derivation of deviatoric stress dependency from viscosity and velocity

In 2D, the deviatoric strain rate tensor can be expressed by the velocity gradient and becomes:

$$\dot{\varepsilon}'_{xx} = \frac{1}{2}\left(\frac{\partial v_x^s}{\partial x} - \frac{\partial v_y^s}{\partial y}\right)$$

(A.20)

$$\dot{\varepsilon}'_{yy} = \frac{1}{2}\left(\frac{\partial v_y^s}{\partial y} - \frac{\partial v_x^s}{\partial x}\right)$$

(A.21)

$$\dot{\varepsilon}'_{xy} = \dot{\varepsilon}'_{yx} = \frac{1}{2}\left(\frac{\partial v_x^s}{\partial y} + \frac{\partial v_y^s}{\partial x}\right)$$

(A.22)

By inserting these expressions in the deviatoric stress-strain rate relationship one finds the following components of the deviatoric stress tensor in function of viscosity and velocity gradient:

$$\sigma'_{xx} = \eta_{xx}^{num}\left(\frac{\partial v_x^s}{\partial x} - \frac{\partial v_y^s}{\partial y}\right) + \sigma_{xx}^{num}$$

(A.23)

$$\sigma'_{yy} = \eta_{yy}^{num}\left(\frac{\partial v_y^s}{\partial y} - \frac{\partial v_x^s}{\partial x}\right) + \sigma_{yy}^{num}$$

(A.24)

$$\sigma'_{xy} = \sigma'_{yx} = \eta^{num}_{(xy|yx)}\left(\frac{\partial v_x^s}{\partial y} + \frac{\partial v_y^s}{\partial x}\right) + \sigma^{num}_{(xy|yx)} \tag{A.25}$$

with η^{num} representing a numerical viscosity given by $\eta^{vp}Z$, $\sigma_{xx}{}^{num} = \sigma'_{xx}{}^0(1 - Z)$, $\sigma_{yy}{}^{num} = \sigma'_{yy}{}^0(1 - Z)$ and $\sigma_{xy}{}^{num} = \sigma_{yx}{}^{num} = \sigma'_{xy}{}^0(1 - Z) = \sigma'_{yx}{}^0(1 - Z)$.

A.6. New porosity computation

The new porosity (Eq. (42)) can be easily computed by discretizing Eq. (41) and with simple algebra:

$$\Delta\varphi = \frac{\Delta\ln\left(\frac{1-\varphi}{\varphi}\right)}{\Delta t}$$

$$\Delta\varphi\Delta t = \Delta\ln\left(\frac{1-\varphi}{\varphi}\right)$$

$$\Delta\varphi\Delta t = \ln\left(\frac{1-\varphi_{new}}{\varphi_{new}}\right) - \ln\left(\frac{1-\varphi}{\varphi}\right) = \ln\left(\frac{1-\varphi_{new}}{\varphi_{new}}\frac{\varphi}{1-\varphi}\right)$$

$$e^{(\Delta\varphi\Delta t)} = \frac{1-\varphi_{new}}{\varphi_{new}}\frac{\varphi}{1-\varphi}$$

$$\frac{(1-\varphi)}{\varphi}e^{(\Delta\varphi\Delta t)} = \frac{1}{\varphi_{new}} - 1$$

$$\frac{(1-\varphi)}{\varphi}e^{(\Delta\varphi\Delta t)} + 1 = \frac{1}{\varphi_{new}}$$

$$\frac{(1-\varphi)e^{(\Delta\varphi\Delta t)} + \varphi}{\varphi} = \frac{1}{\varphi_{new}}$$

$$\varphi_{new} = \frac{\varphi}{(1-\varphi)e^{(\Delta\varphi\Delta t)} + \varphi} \tag{A.26}$$

with Δt the time step, φ_{new} the new porosity and φ the actual porosity on either Lagrangian markers or Eulerian nodes.

A.7. Model resolution test

We assessed the robustness of our SHM numerical solutions by performing a simple model resolution test (Fig. A.1). Six parameters were evaluated during the propagation of the first megathrust earthquake of the modelled seismic cycle. Two model with 1000 m and 500 m grid resolution were compared. Fig. A.1 shows that maximal slip velocity (a) rupture velocity (b), absolute maximal stress (c), total and fluid pressure (d), and effective pressure (e) magnitudes during the rupture, as well as the critical weakening downdip depth reached aseismically before seismic rupture starts (f), remain relatively stable, showing that similarly to previous continuum-based seismic cycle models [Herrendörfer et al., 2018; van Dinther et al., 2013a] the presented results are not significantly dependent on the grid resolution.

References

Audet, P., Schwartz, S.Y., 2013. Hydrologic control of forearc strength and seismicity in the Costa Rican subduction zone. Nat. Geosci. 6 (10), 852. https://doi.org/10.1038/ngeo1927.

Beroza, G.C., Ide, S., 2009. Deep tremors and slow quakes. Science 324 (5930), 1025–1026.

Biot, M.A., 1941. General theory of three-dimensional consolidation. J. Appl. Phys. 12 (2), 155–164. https://doi.org/10.1063/1.1712886.

Biot, M.A., 1956a. Theory of propagation of elastic waves in a fluid-saturated porous solid. I. Low-frequency range. J. Acoust. Soc. Am. 28 (2), 168–178. https://doi.org/10.1121/1.1908239.

Biot, M.A., 1956b. Theory of propagation of elastic waves in a fluid-saturated porous solid. II. Higher frequency range. J. Acoust. Soc. Am. 28 (2), 179–191. https://doi.org/10.1121/1.1908241.

Blaser, L., Kruger, F., Ohrnberger, M., Scherbaum, F., 2010. Scaling relations of earthquake source parameter estimates with special focus on subduction environment. Bull. Seismol. Soc. Am. 100 (6), 2914–2926. https://doi.org/10.1785/0120100111.

Bourbie, T.Z., 1985. Hydraulic and acoustic properties as a function of porosity in Fontainebleau Sandstone. J. Geophys. Res. Solid Earth 90 (B13), 11524–11532. https://doi.org/10.1029/JB090iB13p11524.

Brantut, N., Baker, M., Hansen, L.N., Baud, P., 2018. Microstructural control of physical properties during deformation of porous limestone. J. Geophys. Res. Solid Earth 123 (6), 4751–4764. https://doi.org/10.1029/2018JB015636.

Brown, K.M., Tryon, M.D., DeShon, H.R., Dorman, L.M., Schwartz, S.Y., 2005. Correlated transient fluid pulsing and seismic tremor in the Costa Rica subduction zone. Earth Planet. Sci. Lett. 238 (1), 189–203. https://doi.org/10.1016/j.epsl.2005.06.055.

Cagnioncle, A.M., Parmentier, E.M., Elkins-Tanton, L.T., 2007. Effect of solid flow above a subducting slab on water distribution and melting at convergent plate boundaries. J. Geophys. Res. Solid Earth 112 (B9). https://doi.org/10.1029/2007JB004934. (n/a-n/a).

Carman, P.C., 1939. Permeability of saturated sands, soils and clays. J. Agric. Sci. 29 (2),

262–273. https://doi.org/10.1017/S0021859600051789.

Coelho, G., Branquet, Y., Sizaret, S., Arbaret, L., Champallier, R., Rozenbaum, O., 2015. Permeability of sheeted dykes beneath oceanic ridges: Strain experiments coupled with 3D numerical modeling of the Troodos Ophiolite, Cyprus. Tectonophysics 644-645, 138–150. https://doi.org/10.1016/j.tecto.2015.01.004.

Connolly, J.A.D., 1997. Devolatilization-generated fluid pressure and deformation-propagated fluid flow during prograde regional metamorphism. J. Geophys. Res. Solid Earth 102 (B8), 18149–18173. https://doi.org/10.1029/97JB00731.

Connolly, J.A.D., Podladchikov, Y.Y., 1998. Compaction-driven fluid flow in viscoelastic rock. Geodin. Acta 11 (2–3), 55–84. https://doi.org/10.1016/S0985-3111(98)80006-5.

Connolly, J.A.D., Podladchikov, Y.Y., 2000. Temperature-dependent viscoelastic compaction and compartmentalization in sedimentary basins. Tectonophysics 324 (3), 137–168. https://doi.org/10.1016/S0040-1951(00)00084-6.

Connolly, J.A.D., Podladchikov, Y.Y., 2007. Decompaction weakening and channeling instability in ductile porous media: Implications for asthenospheric melt segregation. J. Geophys. Res. Solid Earth 112 (B10), 15. https://doi.org/10.1029/2005jb004213.

Connolly, J.A.D., Podladchikov, Y.Y., 2015. An analytical solution for solitary porosity waves: dynamic permeability and fluidization of nonlinear viscous and viscoplastic rock. Geofluids 15 (1–2), 269–292. https://doi.org/10.1111/gfl.12110.

Crameri, F., Schmeling, H., Golabek, G.J., Duretz, T., Orendt, R., Buiter, S.J.H., May, D.A., Kaus, B.J.P., Gerya, T.V., Tackley, P.J., 2012. A comparison of numerical surface topography calculations in geodynamic modelling: an evaluation of the 'sticky air' method. Geophys. J. Int. 189 (1), 38–54. https://doi.org/10.1111/j.1365-246X.2012.05388.x.

Dal Zilio, L., van Dinther, Y., Gerya, T.V., Pranger, C.C., 2018. Seismic behaviour of mountain belts controlled by plate convergence rate. Earth Planet. Sci. Lett. 482, 81–92. https://doi.org/10.1016/j.epsl.2017.10.053.

Dal Zilio, L., van Dinther, Y., Gerya, T., Avouac, J.-P., 2019. Bimodal seismicity in the Himalaya controlled by fault friction and geometry. Nat. Commun. 10 (1), 48. https://doi.org/10.1038/s41467-018-07874-8.

David, C., Wong, T.-F., Zhu, W., Zhang, J., 1994. Laboratory measurement of compaction-induced permeability change in porous rocks: implications for the generation and

maintenance of pore pressure excess in the crust. Pageoph 143 (1), 425–456. https://doi.org/10.1007/BF00874337.

Dieterich, J.H., 1979. Modeling of rock friction: 1. Experimental results and constitutive equations. J. Geophys. Res. Solid Earth 84 (B5), 2161–2168. https://doi.org/10.1029/JB084iB05p02161.

van Dinther, Y., Gerya, T.V., Dalguer, L.A., Corbi, F., Funiciello, F., Mai, P.M., 2013a. The seismic cycle at subduction thrusts: 2. Dynamic implications of geodynamic simulations validated with laboratory models. J. Geophys. Res. Solid Earth 118 (4), 1502–1525. https://doi.org/10.1029/2012JB009479.

van Dinther, Y., Gerya, T.V., Dalguer, L.A., Mai, P.M., Morra, G., Giardini, D., 2013b. The seismic cycle at subduction thrusts: Insights from seismo-thermo-mechanical models. J. Geophys. Res. Solid Earth 118 (12), 6202.

van Dinther, Y., Mai, P.M., Dalguer, L.A., Gerya, T.V., 2014. Modeling the seismic cycle in subduction zones: the role and spatiotemporal occurrence of off-megathrust earthquakes. Geophys. Res. Lett. 41 (4), 1201.

Drucker, D.C., Prager, W., 1952. Soil mechanics and plastic analysis of limit design. Q. Appl. Math. 10, 157–165.

Duan, B., Oglesby, D.D., 2005. The dynamics of thrust and normal faults over multiple earthquake cycles: effects of dipping fault geometry. Bull. Seismol. Soc. Am. 95 (5), 1623–1636. https://doi.org/10.1785/0120040234.

Duretz, T., Gerya, T.V., Kaus, B.J.P., Andersen, T.B., 2012. Thermomechanical modeling of slab eduction. J. Geophys. Res. Solid Earth 117 (B8). https://doi.org/10.1029/2012JB009137.

Dymkova, D., Gerya, T., 2013. Porous fluid flow enables oceanic subduction initiation on Earth. Geophys. Res. Lett. 40 (21), 5676.

Gao, X., Wang, K., 2017. Rheological separation of the megathrust seismogenic zone and episodic tremor and slip. Nature 543 (7645), 416–419. https://doi.org/10.1038/nature21389.

Garagash, D.I., 2012. Seismic and aseismic slip pulses driven by thermal pressurization of pore fluid. J. Geophys. Res. Solid Earth 117 (B4). https://doi.org/10.1029/2011JB008889. (n/a-n/a).

Ge, S., Screaton, E., 2005. Modeling seismically induced deformation and fluid flow in the Nankai subduction zone. Geophys. Res. Lett. 32 (17). https://doi.org/10.1029/2005GL023473.

Gerya, T., 2019. Introduction to Numerical Geodynamic Modelling, 2nd ed. Cambridge University Press, Cambridge. https://doi.org/10.1017/9781316534243.

Gerya, T., Yuen, D.A., 2007. Robust characteristics method for modelling multiphase visco-elasto-plastic thermo-mechanical problems. Phys. Earth Planet. Inter. 163 (1–4), 83–105. https://doi.org/10.1016/j.pepi.2007.04.015.

Gerya, T., Stöckhert, B., Perchuk, A.L., 2002. Exhumation of high-pressure metamorphic rocks in a subduction channel: a numerical simulation. Tectonics 21 (6), 6–1–6–19. https://doi.org/10.1029/2002TC001406.

Gueguen, Y., Dienes, J., 1989. Transport properties of rocks from statistics and percolation. Math. Geol. 21 (1), 1–13. https://doi.org/10.1007/BF00897237.

Hamiel, Y., Lyakhovsky, V., Agnon, A., 2005. Rock dilation, nonlinear deformation, and pore pressure change under shear. Earth Planet. Sci. Lett. 237 (3), 577–589. https://doi.org/10.1016/j.epsl.2005.06.028.

Herrendörfer, R., Van Dinther, Y., Gerya, T., Dalguer, L.A., 2015. Earthquake supercycle in subduction zones controlled by the width of the seismogenic zone. Nat. Geosci. https://doi.org/10.1038/ngeo2427.

Herrendörfer, R., Gerya, T., Dinther, Y., 2018. An invariant rate- and state-dependent friction formulation for viscoeastoplastic earthquake cycle simulations. J. Geophys. Res. Solid Earth 123. https://doi.org/10.1029/2017JB015225.

Hughes, K.L.H., Masterlark, T., Mooney, W.D., 2010. Poroelastic stress-triggering of the 2005 M8.7 Nias earthquake by the 2004 M9.2 Sumatra–Andaman earthquake. Earth Planet. Sci. Lett. 293 (3), 289–299. https://doi.org/10.1016/j.epsl.2010.02.043.

Husen, S., Kissling, E., 2001. Postseismic fluid flow after the large subduction earthquake of Antofagasta, Chile. Geology 29 (9), 847–850. https://doi.org/10.1130/0091-7613(2001)029<0847:PFFATL>2.0.CO2.

Ide, S., Beroza, G.C.S., David, R., Uchide, T., 2007. A scaling law for slow earthquakes. Nature 447 (7140), 76. https://doi.org/10.1038/nature05780.

Iwamori, H., 1998. Transportation of H2O and melting in subduction zones. Earth Planet. Sci. Lett. 160 (1), 65–80. https://doi.org/10.1016/S0012-821X(98)00080-6.

Iwamori, H., 2000. Deep subduction of H2O and deflection of volcanic chain towards backarc near triple junction due to lower temperature. Earth Planet. Sci. Lett. 181 (1), 41–46. https://doi.org/10.1016/S0012-821X(00)00180-1.

Iwamori, H., 2007. Transportation of H 2O beneath the Japan arcs and its implications for global water circulation. Chem. Geol. 239 (3), 182–198. https://doi.org/10.1016/j.chemgeo.2006.08.011.

Jaeger, J.C., Cook, N.G.W., Zimmerman, R., 2007. Fundamentals of Rock Mechanics, 4th ed. Wiley-Blackwell 489 pp.

Kaneko, Y., Avouac, J.-P., Lapusta, N., 2010. Towards inferring earthquake patterns from geodetic observations of interseismic coupling. Nat. Geosci. 3 (5), 363. https://doi.org/10.1038/ngeo843.

Katz, R.F., Spiegelman, M., Holtzman, B., 2006. The dynamics of melt and shear localization in partially molten aggregates. Nature 442 (7103), 676–679.

Kaus, B.J.P., 2010. Factors that control the angle of shear bands in geodynamic numerical models of brittle deformation. Tectonophysics 484 (1), 36–47. https://doi.org/10.1016/j.tecto.2009.08.042.

Keller, T., May, D.A., Kaus, B.J.P., 2013. Numerical modelling of magma dynamics coupled to tectonic deformation of lithosphere and crust. Geophys. J. Int. 195 (3), 1406–1442. https://doi.org/10.1093/gji/ggt306.

Koulakov, I., West, M., Izbekov, P., 2013. Fluid ascent during the 2004–2005 unrest at Mt. Spurr inferred from seismic tomography. Geophys. Res. Lett. 40 (17), 4579–4582. https://doi.org/10.1002/grl.50674.

LaBonte, A.L., Brown, K.M., Fialko, Y., 2009. Hydrologic detection and finite element

modeling of a slow slip event in the Costa Rica prism toe. J. Geophys. Res. Solid Earth 114 (B4). https://doi.org/10.1029/2008JB005806.

Lapusta, N., Liu, Y., 2009. Three-dimensional boundary integral modeling of spontaneous earthquake sequences and aseismic slip. J. Geophys. Res. Solid Earth 114 (B9). https://doi.org/10.1029/2008JB005934. (n/a-n/a).

Lapusta, N., Rice, J.R., Ben-Zion, Y., Zheng, G., 2000. Elastodynamic analysis for slow tectonic loading with spontaneous rupture episodes on faults with rate- and state-dependent friction. J. Geophys. Res. Solid Earth 105 (B10), 765–789. https://doi.org/10.1029/2000JB900250.

Lavier, L.L., Buck, R.W., Poliakov, A.N.B., 2000. Factors controlling normal fault offset in an ideal brittle layer. J. Geophys. Res. Solid Earth 105 (B10), 23431–23442. https://doi.org/10.1029/2000JB900108.

Liu, Y., Rice, J.R., 2007. Spontaneous and Triggered Aseismic Deformation Transients in a Subduction Fault Model. https://doi.org/10.1029/2007JB004930.

Liu, Y., Rice, J.R., 2009. Slow Slip Predictions Based on Granit and Gabbro Friction Data Compared to GPS Measurements in Northern Cascadia. https://doi.org/10.1029/2008JB006142.

Lockner, D.A., Stanchits, S.A., 2002. Undrained poroelastic response of sandstones to deviatoric stress change. J. Geophys. Res. Solid Earth 107 (B12). https://doi.org/10.1029/2001JB001460. (ETG 13–11-ETG 13–14).

Lu, G., Wang, X., Li, F., Xu, F., Wang, Y., Qi, S., Yuen, D., 2017. Deep geothermal processes acting on faults and solid tides in coastal Xinzhou geothermal field, Guangdong, China. Phys. Earth Planet. Inter. 264, 76–88. https://doi.org/10.1016/j.pepi.2016.12.004.

Mavko, G., Mukerji, T., Dvorkin, J., 2009. The Rock Physics Handbook: Tools for Seismic Analysis of Porous Media. Cambridge university press.

McKenzie, D.A.N., 1984. The generation and compaction of partially molten rock. J. Petrol. 25 (3), 713–765.

Mitsui, N., Kato, N., Fukahata, Y., Hirahara, K., 2012. Megaquake cycle at the Tohoku subduction zone with thermal fluid pressurization near the surface. Earth Planet. Sci. Lett. 325 (326), 21.

Morency, C., Huismans, R.S., Beaumont, C., Fullsack, P., 2007. A numerical model for coupled fluid flow and matrix deformation with applications to disequilibrium compaction and delta stability. J. Geophys. Res. Solid Earth 112 (B10). https://doi.org/10.1029/2006jb004701.

Moreno, M., Haberland, C., Oncken, O., Rietbrock, A., Angiboust, S., Heidbach, O., 2014. Locking of the Chile subduction zone controlled by fluid pressure before the 2010 earthquake. Nat. Geosci. 7 (4), 292–296. https://doi.org/10.1038/ngeo2102.

Moreno, M., et al., 2018. Chilean megathrust earthquake recurrence linked to frictional contrast at depth. Nat. Geosci. 11 (4), 285–290. https://doi.org/10.1038/s41561-018-0089-5.

Nakajima, J., Uchida, N., 2018. Repeated drainage from megathrusts during episodic slow slip. Nat. Geosci. https://doi.org/10.1038/s41561-018-0090-z.

Noda, H., Lapusta, N., 2010. Three-dimensional earthquake sequence simulations with evolving temperature and pore pressure due to shear heating: Effect of heterogeneous hydraulic diffusivity. J. Geophys. Res. Solid Earth 115 (B12). https://doi.org/10.1029/2010JB007780. (n/a-n/a).

Obara, K., 2002. Nonvolcanic deep tremor associated with subduction in Southwest Japan. (reports).(seismological research)(Statistical Data included). Science 296 (5573), 1679.

Pacheco, J.F., Sykes, L.R., 1992. Seismic moment catalog of large shallow earthquakes, 1900 to 1989. Bull. Seismol. Soc. Am. 82 (3), 1306–1349.

Peng, Z., Gomberg, J., 2010. An integrated perspective of the continuum between earthquakes and slow-slip phenomena. Nat. Geosci. 3 (9), 599. https://doi.org/10.1038/ngeo940.

Poulet, T., Veveakis, E., Regenauer-Lieb, K., Yuen, D.A., 2014. Thermo-poro-mechanics of chemically active creeping faults: 3. The role of serpentinite in episodic tremor and slip sequences, and transition to chaos. J. Geophys. Res. Solid Earth 119 (6), 4606–4625. https://doi.org/10.1002/2014JB011004.

Poulet, T., Paesold, M., Veveakis, M., 2017. Multi-physics modelling of fault mechanics using REDBACK: a parallel open-source simulator for tightly coupled problems. Rock Mech. Rock. Eng. 50 (3), 733–749. https://doi.org/10.1007/s00603-016-0927-y.

Preuss, S., Herrendörfer, R., Gerya, T., Ampuero, J.-P., van Dinther, Y., 2019. Seismic and aseismic fault growth lead to different fault orientations. J. Geophys. Res. Solid Earth 124 (8), 8867–8889. https://doi.org/10.1029/2019JB017324.

Ranalli, G., 1995. Rheology of the Earth. Springer.

Rice, J.R., 1992. Fault stress states, pore pressure distributions, and the weakness of the San Andreas Fault. Int. Geophys. 51 (C), 475–503. https://doi.org/10.1016/S0074-6142(08)62835-1.

Romanet, P., Bhat Harsha, S., Jolivet, R., Madariaga, R., 2018. Fast and slow slip events emerge due to fault geometrical complexity. Geophys. Res. Lett. 45 (10), 4809–4819. https://doi.org/10.1029/2018GL077579.

Ruina, A., 1983. Slip instability and state variable friction laws. J. Geophys. Res. Solid Earth 88 (B12), 10359–10370. https://doi.org/10.1029/JB088iB12p10359.

Rutqvist, J., Figueiredo, B., Hu, M., Tsang, C.-F., 2018. Chapter 7 - Continuum modeling of hydraulic fracturing in complex fractured rock masses. In: Wu, Y.-S. (Ed.), Hydraulic Fracture Modeling. Gulf Professional Publishing, pp. 195–217. https://doi.org/10.1016/B978-0-12-812998-2.00007-2.

Saffer, D.M., Tobin, H.J., 2011. Hydrogeology and mechanics of subduction zone forearcs: fluid flow and pore pressure. In: Annu. Rev. Earth Planet. Sci, pp. 157–186. https://doi.org/10.1146/annurev-earth-040610-133408.

Saffer, D.M., Wallace, L.M., 2015. The frictional, hydrologic, metamorphic and thermal habitat of shallow slow earthquakes. Nat. Geosci. 8 (8), 594–600. https://doi.org/10.1038/ngeo2490.

Schmeling, H., et al., 2008. A benchmark comparison of spontaneous subduction models—towards a free surface. Phys. Earth Planet. Inter. 171 (1), 198–223. https://doi.

org/10.1016/j.pepi.2008.06.028.

Schmeling, H., Kruse, J.P., Richard, G., 2012. Effective shear and bulk viscosity of partially molten rock based on elastic moduli theory of a fluid filled poroelastic medium. Geophys. J. Int. 190 (3), 1571–1578. https://doi.org/10.1111/j.1365-246X.2012.05596.x.

Segall, P., Rice, J.R., 1995. Dilatancy, compaction, and slip instability of a fluid-infiltrated fault. J. Geophys. Res. Solid Earth 100 (B11), 22155–22171. https://doi.org/10.1029/95JB02403.

Segall, P., Rice, J.R., 2006. Does shear heating of pore fluid contribute to earthquake nucleation? J. Geophys. Res. Solid Earth 111 (B9). https://doi.org/10.1029/2005JB004129. (n/a-n/a).

Shapiro, S.A., 2015. Fluid-Induced Seismicity. Cambridge University Press, Cambridge. https://doi.org/10.1017/CBO9781139051132.

Shapiro, S.A., Dinske, C., 2009. Fluid-induced seismicity: pressure diffusion and hydraulic fracturing. Geophys. Prospect. 57 (2), 301–310. https://doi.org/10.1111/j.1365-2478.2008.00770.x.

Shapiro, S.A., Patzig, R., Rothert, E., Rindschwentner, J., 2003. Triggering of seismicity by pore-pressure perturbations: permeability-related signatures of the phenomenon. Pageoph 160 (5), 1051–1066. https://doi.org/10.1007/PL00012560.

Sibson, R.H., 1990. Faulting and fluid flow. In: Fluids in Tectonically Active Regimes of the Continental Crust. Mineralogical Association of Canada, Vancouver, pp. 93–132.

Skarbek, R.M., Rempel, A.W., 2016. Dehydration-induced porosity waves and episodic tremor and slip. Geochem. Geophys. Geosyst. 17 (2), 442–469. https://doi.org/10.1002/2015GC006155.

Sleep, N.H., Blanpied, M.L., 1994. Ductile creep and compaction: a mechanism for transiently increasing fluid pressure in mostly sealed fault zones. Pure Appl. Geophys. 143 (1), 9–40. https://doi.org/10.1007/BF00874322.

Sobolev, S.V., Muldashev, I.A., 2017. Modeling seismic cycles of great megathrust earthquakes across the scales with focus at postseismic phase. Geochem. Geophys. Geosyst. https://doi.org/10.1002/2017GC007230. (n/a-n/a).

Spiegelman, M., 1993. Flow in deformable porous media. Part 1 simple analysis. J. Fluid Mech. 247, 17–38. https://doi.org/10.1017/S0022112093000369.

Stevenson, D.J., Scott, D.R., 1991. Mechanics of fluid-rock systems. Annu. Rev. Fluid Mech. 23 (1), 305–339. https://doi.org/10.1146/annurev.fl.23.010191.001513.

Tassara, A., Soto, H., Bedford, J., Moreno, M., Baez, J.C., 2016. Contrasting amount of fluids along the megathrust ruptured by the 2010 Maule earthquake as revealed by a combined analysis of aftershocks and afterslip. Tectonophysics 671, 95–109. https://

doi.org/10.1016/j.tecto.2016.01.009.

Templeton, E.L., Rice, J.R., 2008. Off-fault plasticity and earthquake rupture dynamics: 1. Dry materials or neglect of fluid pressure changes. J. Geophys. Res. Solid Earth 113 (B9). https://doi.org/10.1029/2007JB005529.

Vermeer, P.A., de Borst, R., 1984. Non-associated plasticity for soils, concrete and rock. HERON 29 (3).

Viesca, R.C., Templeton, E.L., Rice, J.R., 2008. Off-fault plasticity and earthquake rupture dynamics: 2. In: Effects of Fluid Saturation, https://doi.org/10.1029/2007JB005530.

Wang, J., 1984. Young's modulus of porous materials. J. Mater. Sci. 19 (3), 809–814. https://doi.org/10.1007/BF00540452.

Wang, K., 2007. Elastic and Viscoelastic Models of Crustal Deformation in Subduction Earthquake Cycles (540 pp). Columbia University Press, New York.

Wang, K., Hu, Y., He, J., 2012. Deformation cycles of subduction earthquakes in a viscoelastic Earth. Nature 484 (7394), 327. https://doi.org/10.1038/nature11032.

Wilson, C.R., Spiegelman, M., van Keken, P.E., Hacker, B.R., 2014. Fluid flow in subduction zones: the role of solid rheology and compaction pressure. Earth Planet. Sci. Lett. 401, 261–274. https://doi.org/10.1016/j.epsl.2014.05.052.

Wong, T.-F., Baud, P., 2012. The brittle-ductile transition in porous rock: a review. J. Struct. Geol. 44, 25–53. https://doi.org/10.1016/j.jsg.2012.07.010.

Yamashita, T., Suzuki, T., 2011. Dynamic modeling of slow slip coupled with tremor. J. Geophys. Res. Solid Earth 116 (B5). https://doi.org/10.1029/2010JB008136. (n/a-n/a).

Yarushina, V.M., Minakov, A., 2018. Wave propagation in porous elastoplastic rocks: implication for seismic attenuation. In: EAGE 2016 Conference.

Yarushina, V.M., Podladchikov, Y.Y., 2015. (De)compaction of porous viscoelastoplastic media: model formulation. J. Geophys. Res. Solid Earth 120 (6), 4146–4170. https://doi.org/10.1002/2014JB011258.

Yarushina, V.M., Bercovici, D., Oristaglio, M.L., 2013. Rock deformation models and fluid leak-off in hydraulic fracturing. Geophys. J. Int. 194 (3), 1514–1526. https://doi.org/10.1093/gji/ggt199.

Yarushina, V.M., Podladchikov, Y.Y., Connolly, J.A.D., 2015. (De)compaction of porous viscoelastoplastic media: solitary porosity waves. J. Geophys. Res. Solid Earth 120 (7), 4843–4862. https://doi.org/10.1002/2014JB011260.

Yarushina, V.M., Podladchikov Yuri, Y., Minakov, A., Räss, L., 2017. On the mechanisms of stress-triggered seismic events during fluid injection. Poromechanics VI 795–800. https://doi.org/10.1061/9780784480779.09810.1061/9780784480779.098.